ADVANCING EARTH AND SPACE SCIENCES

JGR Solid Earth

RESEARCH ARTICLE

10.1029/2024JB030663

Special Collection:
Slow to fast earthquakes and the geology, structure, and rheology of their host subduction zones

The Dynamics of Fast and Slow Earthquake Ruptures in Viscoelastic Materials

Huihui Weng[1]

[1]State Key Laboratory of Critical Earth Material Cycling and Mineral Deposits, School of Earth Sciences and Engineering, Nanjing University, Nanjing, China

Key Points:

- Ruptures in viscoelastic materials can propagate steadily at a terminal speed that spans a continuum range of values
- A new fracture mechanics theory incorporating viscoelasticity can predict all simulated rupture speeds
- The effects of viscoelasticity cannot be ignored in earthquake rupture propagation, even within narrow fault zones

Correspondence to:

H. Weng,
weng@nju.edu.cn

Citation:

Weng, H. (2025). The dynamics of fast and slow earthquake ruptures in viscoelastic materials. *Journal of Geophysical Research: Solid Earth*, *130*, e2024JB030663. https://doi.org/10.1029/2024JB030663

Received 29 OCT 2024
Accepted 25 MAY 2025

Author Contributions:

Conceptualization: Huihui Weng
Data curation: Huihui Weng
Formal analysis: Huihui Weng
Funding acquisition: Huihui Weng
Investigation: Huihui Weng
Methodology: Huihui Weng
Project administration: Huihui Weng
Resources: Huihui Weng
Software: Huihui Weng
Supervision: Huihui Weng
Validation: Huihui Weng
Visualization: Huihui Weng
Writing – original draft: Huihui Weng
Writing – review & editing: Huihui Weng

Abstract

Classical theories using linear elasticity predict that crack propagation asymptotically approaches a limiting speed, beyond which the energy balance becomes unphysical. However, geophysical and laboratory observations show that ruptures can propagate at either a very low, stable speed or a significantly high speed. Here, we first use numerical simulations to show that frictional ruptures in viscoelastic materials can steadily propagate at a terminal speed, rather than asymptotically approaching the classical speed limit. The simulated terminal speed spans a continuum of values, ranging from slow ruptures to supershear ruptures. We then develop a new theory incorporating viscoelasticity to predict all simulated rupture speeds. In addition to the ratio of fracture energy to static energy release rate, we find that three length scales also play a crucial role in governing the energy balance during rupture in viscoelastic materials. The theory predicts that stable rupture speeds are energetically allowed to be very small, which helps explain the widespread occurrence of slow earthquakes. Beyond the classical speed limit, the energy balance becomes independent of macroscopic length scales, being controlled solely by the local properties around the rupture tip. Furthermore, we find that the effects of viscoelasticity in fault zones are significant in earthquake rupture propagation, even when the fault-zone geometrical scales are short relative to other fault dimensions. These numerical and theoretical findings fundamentally advance our understanding of dynamic rupture propagation.

Plain Language Summary

Classical theories based on linear elasticity predict that crack propagation asymptotically approaches a limiting speed, which contradicts observations from both laboratory experiments and natural earthquakes. In this study, we introduce a frictional rupture model in viscoelastic rocks, demonstrating that viscoelastic materials can maintain a steady terminal speed, rather than asymptotically approaching the classical speed limit. The simulated terminal speed spans a continuum of values, ranging from slow ruptures to supershear ruptures. Our computational results agree with a newly developed analytical model based on energy balance. Furthermore, this study highlights the critical role of viscoelasticity in narrow fault damage zones, even when its thickness is much smaller than other fault dimensions.

1. Introduction

The mechanism controlling crack propagation speeds is of critical interest to Earth science communities and has significant technological applications. Classical fracture mechanics theories (Freund, 1998) based on two-dimensional (2D) linear elasticity predict that crack propagation is bounded by a limiting speed: Rayleigh-wave speed in tensile cracks (Mode I), P-wave speed in in-plane shear cracks (Mode II), and S-wave speed in anti-plane shear cracks (Mode III). Because the energy flux into a crack tip drops to 0 as the crack propagation speed approaches the speed limit and becomes negative beyond the speed limit, the energy balance solution is physical only for speeds lower than the speed limit. The prediction of classical speed limits has been confirmed experimentally (Kammer et al., 2018; Svetlizky et al., 2019) and numerically (Andrews, 1976) based on materials with linear elastic behavior. Since the energy release rate is also an increasing function of the crack length in a 2D elastic framework (Freund, 1998), spontaneous cracks, controlled by the energy balance, asymptotically approach the speed limit as the crack length increases. In light of this energetic nature, achieving a steady state rupture in 2D requires additional frictional complexities, such as self-healing frictional behaviors (Dong et al., 2023; Rice et al., 2005) that leads to pulse-like ruptures instead of cracks.

Recent developments (Weng & Ampuero, 2019, 2020, 2022) have extended the classical 2D elastic crack theory to a 3D framework by incorporating a finite rupture width, a crucial condition controlling large crustal earthquakes (Scholz, 1998; Weng & Yang, 2017) whose rupture length exceeds the seismogenic width (Figure 1a).

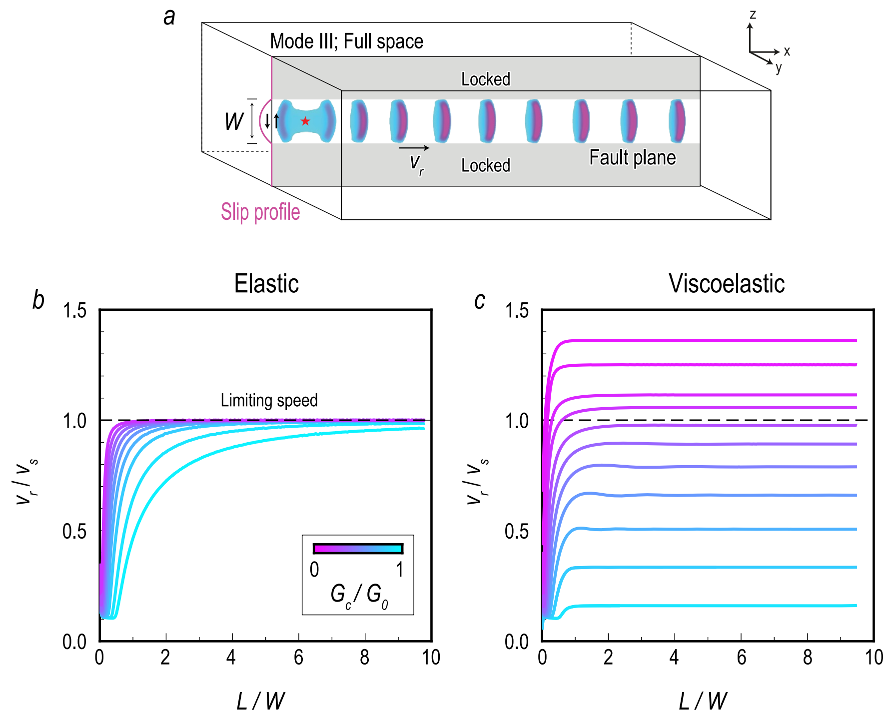

Figure 1. Rupture propagation on a long fault embedded in full-space elastic and viscoelastic media. (a) Sketch of the geometry, where a frictional rupture is confined within a vertical planar fault with finite width W and vertical homogeneous shear loading (Mode III). The colors on the fault plane indicate that frictional rupture starts from the red star and propagates horizontally as a pulse. (b) Normalized rupture speed v_r/v_s as a function of the normalized rupture distance L/W from the elastic models. The colored curves are coded by the energy ratio G_c/G_0. v_s is the limiting shear wave speed. (c) Colored curves are the same as those in (b) but from the viscoelastic models with $\eta v_s/W = 1/75$. Note that the minimum simulated rupture speed in this study is $\sim 0.01 v_s$, which is not shown here.

The primary difference in 3D theory is that the elastic energy release rate depends on the finite rupture width rather than the length (Weng & Ampuero, 2019), which leads to pulse-like ruptures without the need for additional complexities related to fault friction. This 3D problem of elongated frictional ruptures is fundamentally analogous to the 2D problem of tensile cracks in strips (Goldman et al., 2010; Marder, 1998; Thøgersen et al., 2021), snow slab avalanches (Trottet et al., 2022), and the classical PKN (Perkins–Kern–Nordgren) model of hydraulic fracture (Kovalyshen & Detournay, 2009), whose energy release rates are also confined by width. Because the energy release rate does not increase with rupture length in 3D theory, steady-state solutions are mathematically inferred (Weng & Ampuero, 2019); but a physically steady-state rupture requires additional stabilization conditions (Weng & Ampuero, 2022). For instance, steady-state ruptures with a constant terminal speed have been numerically validated and quantitatively predicted by incorporating transient frictional strengthening (Weng & Ampuero, 2022) and slip obliqueness (mixed mode) (Weng & Ampuero, 2020). The feasible rupture speeds in elastic media are still restricted by classical speed limits.

In addition to widely observed fast earthquakes, which typically have rupture speeds greater than one-third of the S-wave speed (Chounet et al., 2018), slow earthquakes of various time and spatial scales have also been observed in natural faults worldwide (Hirose et al., 1999; Ide et al., 2007; Ito et al., 2007; Katsumata & Kamaya, 2003; Obara, 2002). Specifically, there is a type of slow-slip rupture phenomenon, known as slow slip events (SSEs), that lasts from several weeks to several years and extends over tens to hundreds of kilometers (Beroza & Ide, 2011). SSEs usually unzip an elongated section of the deep plate interface, resulting in elongated ruptures with finite widths (Houston et al., 2011; Michel et al., 2019), and their rupture speeds can be several orders of magnitude slower than the S wave speed (Weng & Ampuero, 2022). Liu and Rice (2005) suggested that a critical nucleation size with length scales close to the fault width can generate transient slow slip events. But the resulting range of rupture speeds of SSEs under this condition is much narrower than that observed globally (Liu & Rice, 2005; Weng & Ampuero, 2022), and the resulting SSEs are not steady-state ruptures (Dal Zilio et al., 2020).

10.1029/2024JB030663

To explain a wider range of rupture speeds, numerical simulations are conducted by considering fault geometric complexities (Cattania & Segall, 2021), frictional complexities (Hawthorne & Rubin, 2013; Luo & Liu, 2021; Shibazaki & Iio, 2003), material constitutive complexities (Ando et al., 2012; Beall et al., 2019; Behr & Bürgmann, 2021; Behr et al., 2021; Behr et al., 2018; Lavier et al., 2021; Ujiie et al., 2018), and fault gouge dilatancy with fluids (Liu & Rubin, 2010; Segall et al., 2010; Suzuki & Yamashita, 2009). Despite these studies using fault interface and inelastic constitutive complexities to explain slow earthquakes, a fundamental theory of inelastic ruptures that enables the explanation of both fast and slow ruptures remains lacking.

Experiments with viscoelastic polymers demonstrated that tensile cracks (Mai et al., 2020; Petersan et al., 2004; Wang et al., 2023) can surpass the S-wave speed—known as supershear ruptures—and that frictional ruptures (Gori et al., 2018) in Mode II can surpass the P-wave speed—known as supersonic ruptures. Additionally, supersonic ruptures have also been reported in 2D simulations of hyperelastic materials (Buehler et al., 2003; Chen et al., 2017; Gumbsch & Gao, 1999; Guozden et al., 2010; Marder, 2005), where small scales of hyperelasticity can play a crucial role in dynamic rupture propagation. Although supersonic ruptures have been reported in experiments and simulations, validating their existence in natural earthquakes is still challenging, primarily due to uncertainties in constraining their rupture speeds and the velocities of the hosting media at seismogenic depths (Chounet et al., 2018). These reported supershear and supersonic ruptures cannot be explained by classical 2D theories based on linear elasticity. Contrast to the assumption of linear elasticity, many materials, including rocks (Fan et al., 2011; Yan et al., 2022; Q. B. Zhang & Zhao, 2013) and polymers (Gori et al., 2018), exhibit obvious viscoelastic behavior. In addition, the strong attenuation observed within natural fault damage zones suggests viscoelastic behavior (e.g., H. Zhang et al., 2023), although it remains challenging to quantitatively compare the velocity dispersion of fault zones with a constitutive model.

Fracture in 2D viscoelastic materials has gained attentions for engineering purposes (Knauss, 2015; Rodriguez et al., 2021) and the energy balance analyses for tensile cracks in both 2D viscoelastic infinite (Carbone & Persson, 2005; Greenwood & Johnson, 1981; Hui et al., 1992; Nagatakiya et al., 2023; Persson & Brener, 2005; Saulnier et al., 2004) and finite (Barber et al., 1989; Langer, 1992; Seshadri et al., 2007; Willis, 1967; Xu et al., 1992) plates have been developed. However, in existing 2D viscoelastic crack theories, little emphasis is placed on slow ruptures and supershear rupture—a subject of particular interest to the Seismology Community. Additionally, there is still a theoretical gap in understanding frictional ruptures occurring on elongated faults embedded in 3D viscoelastic materials and their analytical rupture tip equation of motion has yet to be developed and validated via dynamic rupture simulations. In this study, we first present the numerical models in Section 2 and the simulated results featuring a continuum of terminal speeds in Section 3. We then present new fracture mechanics theories that consider either linear elastic or viscoelastic materials in Section 4 and quantitatively compare the theoretical predictions with the numerical results in Section 5. Finally, we discuss the scope of this study in Section 6.

2. Numerical Models

In this study, we consider frictional rupture propagation on a shear loading fault (Mode III) with a sufficiently long length and a finite width W, embedded in a full-space homogeneous isotropic medium (Figure 1a). This model is referred to as the 3D elongated rupture problem, which has been successfully approximated in elastic media by a 2.5D reduced model that accounts for elongated features while significantly reducing computational costs (Johnson, 1992; Lapusta, 2001; Weng & Ampuero, 2019, 2022). Thus, most of the presented results in this study are simulated using the 2.5D model, while a few 3D and 2D models are also conducted for quantitative comparison with the 2.5D models. Both elastic and Kelvin–Voigt viscoelastic materials are considered in this study. The shear modulus, S-wave speed, and P-wave speed of the medium are denoted as μ, v_s, and v_p, respectively. The retardation time of Kelvin–Voigt viscoelastic media, the ratio of viscosity to shear modulus, is denoted η with unit of seconds. Note that the retardation time of Kelvin–Voigt viscoelasticity reflects a dynamic aspect of material response to stress and strain, differing from the relaxation time of Maxwell viscoelasticity, which provides a better representation of long-term crustal deformation. Although Kelvin–Voigt viscoelasticity may be inadequate at the very high-frequency regime, we use this model in this study for two reasons: first, the rock experiments (Fan et al., 2011; Yan et al., 2022; Q. B. Zhang & Zhao, 2013), polymer experiments (Gori et al., 2018), and viscoelastic attenuation of fault damage zones (H. Zhang et al., 2023) all support this model, and second, this model facilitates the mathematical derivations. To numerically simulate the full-space media, a sufficiently large domain and absorbing boundaries are used and the simulation time is set to be shorter than the traveling times of the seismic waves reflected back from the domain boundaries onto the fault. As seismic waves attenuate rapidly for large values of η, the simulation time can be safely extended to simulate slow ruptures without the interference of reflected waves. For direct comparison with the fracture mechanics theory, most of the numerical parameters and simulated results are presented in non-dimensional forms.

To focus on the fundamental features of rupture mechanics, here we consider the simplest linear slip-weakening friction law, where the static strength τ_s, the dynamic strength τ_d, and the slip-weakening distance d_c are prescribed parameters in the simulations (Ida, 1972). The fracture energy of dynamic ruptures is given by $G_c = \frac{1}{2}\tau_c d_c$, where $\tau_c = \tau_s - \tau_d$. In addition, the initial shear stress τ_0 on faults is a prescribed parameter, so the stress drop of ruptures is controlled by $\Delta\tau = \tau_0 - \tau_d$ and the static energy release rate is given by $G_0 = \Delta\tau^2 W/\pi\mu$ in full-space media (Weng & Ampuero, 2019). Note that if $G_c/G_0 > 1$, all ruptures will spontaneously arrest due to insufficient elastic energy to sustain frictional dissipation (Weng & Ampuero, 2019), which is not considered here. In this study, the energy ratio G_c/G_0 is varied between 0.99 and 0.09 for simulating a wide range of rupture speeds v_r. The size of cohesive zone Λ is defined by the length of the fault region behind the rupture tip where the shear stress drops from τ_s to τ_d. The theoretical prediction of the static size of the cohesive zone, Λ_0, in linear elasticity (Palmer & Rice, 1973) is

$$\Lambda_0 = \frac{9\pi}{32}\frac{\mu d_c}{\tau_s - \tau_d}. \tag{1}$$

Since Λ depends on both Λ_0 and v_r, it is thus a measured value from the simulations. In the simulations, Λ_0/W is varied between $1/40$ and $1/20$ and $\eta v_s/W$ is varied between $1/6000$ and $1/24$ for simulating wide ranges of Λ/W and $\eta v_r/W$. To investigate the effects of finite viscoelastic layers, additional models are simulated with viscoelastic properties at $|y| < H/2$ and elastic properties at $|y| > H/2$, where y is the axis normal to the fault and H is the thickness of viscoelastic layer. In the simulations, H/W is varied between 0.025 and 5.

We also simulate 3D and 2D models. Since the 3D simulations are much more expensive than the 2.5D ones, only a few 3D models are simulated for a direct comparison. In the compared models, $\eta v_s/W = 1/250$, $\Lambda_0/W = 1/20$, and G_c/G_0 is varied between 0.09 and 0.7. The domain dimensions of the 3D models are 400km $\times$ 200km $\times$ 220km, with a fault length of 360km and a fault width of $W = 20$km; However, all these lengths can be scaled according to the specific values of Λ_0 and ηv_s to obtain the corresponding non-dimensional ratios. To validate that the energy balance in supershear regime is independent of any macroscopic length, the 2D models are simulated and compared to the 2.5D models. In the 2D models, all parameters are kept the same as those compared 2.5D models except with an infinite fault width (the assumption of classical 2D framework).

The ruptures are forced to start by a prescribed time-weakening nucleation zone of size $L_{nuc}/W = 1$ and speed $v_{nuc}/v_s = 0.1$. Outside the nucleation zone, frictional ruptures are spontaneous and controlled by linear slip-weakening friction law as described above. The spectral element software SEM2DPACK (Ampuero, 2012) is used to simulate the 2.5D and 2D dynamic rupture models and the spectral element software SPECFEM3D (Galvez et al., 2014) is used to simulate the 3D models. The numerical resolution is guaranteed by using sufficiently small grid sizes Δx, which is $\Lambda_0/\Delta x \geq 16$ following Weng and Ampuero (2019). The time step is prescribed based on the Courant-Friedrichs-Lewy stability condition, which decreases as the retardation time increases (Ampuero, 2012). We also test different nucleation speeds and model grid sizes to confirm that neither the nucleation conditions nor the grid sizes affect the simulated steady-state terminal speeds.

3. A Continuum of Terminal Speeds in Numerical Simulations

In the context of linear elasticity, rupture propagation on long faults ($>W$) can be uniquely controlled by adjusting the dimensionless energy ratio (Weng & Ampuero, 2019), G_c/G_0, where G_c is the frictional fracture energy, and $G_0 = \Delta\tau^2 W/\pi\mu$ is the static energy release rate, which is proportional to the square of the stress drop $\Delta\tau$ and W. Another length scale is used in the dynamic rupture simulation, the size of the cohesive zone Λ, though it is insignificant in the elastic rupture tip equations of motion when $\Lambda \ll W$ (Freund, 1998; Weng & Ampuero, 2019). In addition, the viscoelasticity has an intrinsic length scale: the viscous dissipation length ηv_r, where v_r is the

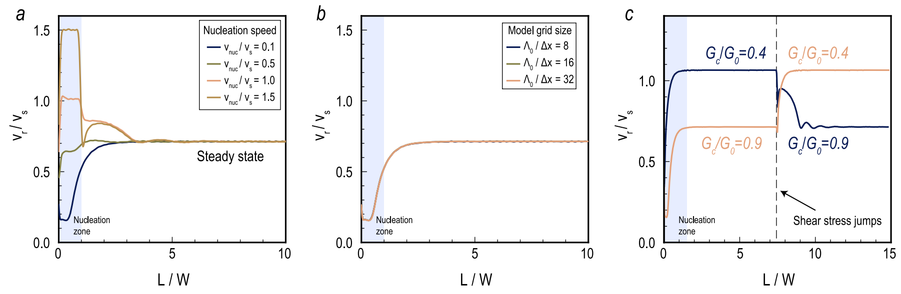

Figure 2. Effects of nucleation speed, model grid size, and shear stress perturbation on rupture propagation. (a–b) Normalized rupture speeds v_r/v_s as a function of the normalized distance L/W, based on the 2.5D models with different time-weakening nucleation speeds (a) and with different model grid sizes (b). (c) The two curves show the transition of ruptures from one steady state to another due to a jump in shear stress at $L/W = 7.5$ (dashed line), with the two segments of different values of G_c/G_0 indicated in the legend. Gray areas indicate the nucleation zone.

steady-state rupture terminal speed. In this study, broad ranges of G_c/G_0, Λ/W, and $\eta v_r/W$ are tested by prescribing various initial parameters in dynamic rupture simulations.

Our numerical results reconfirm that all elastic ruptures asymptotically approach but never exceed the limiting speed v_s in Mode III, no matter how critically the fault is loaded (Figure 1b). During elastic rupture propagation, the size of the cohesive zone, which dissipates the released elastic energy, is physically modulated by the Lorentz contraction factor, $\alpha_s = \sqrt{1 - (v_r/v_s)^2}$ (Section 4.2). The speed limit in terms of elasticity arises because the Lorentz contraction factor decreases to 0 at $v_r = v_s$ and produces unphysical solutions when $v_r > v_s$, analogous to the principles of special relativity. In other words, when the rupture propagation speed exceeds the wave propagation speed, which is constant in elastic materials, the law of cause and effect physically enforces this speed limit for spontaneous ruptures.

In contrast to elastic ruptures, we find that frictional ruptures in viscoelastic materials can steadily propagate at a terminal speed, rather than asymptotically approaching the classical speed limit (Figure 1c). The viscoelastic models can produce a continuum of terminal speeds, ranging from slow ruptures to supershear ruptures, and are not bounded by v_s. Tests show that rupture propagation can be maintained at an intrinsic steady-state speed v_r controlled by G_c/G_0, regardless of the nucleation conditions, model grid sizes, or perturbations of stresses (Figure 2). Generally, v_r increases as G_c/G_0 decreases. If G_c/G_0 is close to 1 from below (i.e., the static energy release rate is slightly greater than the fracture energy), the simulated v_r can be as slow as SSEs, with the minimum simulated rupture speed in this study being $\sim 0.01 v_s$. Note that even slower ruptures can be simulated, but these models require substantial computational costs in dynamic rupture simulation codes and their results are anticipated without providing additional insights. If G_c/G_0 is close to 0 (i.e., the fault is critically loaded), v_r can surpass v_s, and these ruptures smoothly accelerate to steady supershear speeds, which differs from the supershear transition observed in Mode II elastic ruptures (Andrews, 1976; Burridge, 1973). Additional, the simulations in this study do not produce observable oscillations in the supershear speed regime, a phenomenon reported only for tensile cracks (Chen et al., 2017; Wang et al., 2023). This may be because, in simulations of frictional ruptures, a pre-existing fault is assumed to have weaker strength than the surrounding continuum media, as is commonly accepted in the seismological community. This configuration is analogous to the imprinting of weak layers in tensile crack experiments that can suppress oscillations of supershear speeds (Wang et al., 2023). If the strength of the media surrounding fault interfaces is comparable to the fault's frictional strength, such as with granular materials within fault zones (Åström et al., 2000), rupture propagation paths may not be straight, and oscillatory instabilities may emerge in the supershear speed regime.

Mach fronts appear when rupture propagation is faster than wave propagation, similar to the phenomenon of a sonic boom caused by supersonic flight. In the simulations, remarkable Mach fronts are observed in the velocity fields around the rupture tips when $v_r/v_s > 1$ (Figure 3a). The inclination angle θ between the track of peak velocities and the fault line is quantitatively consistent with the theoretical prediction (Figure 3b), $\theta = \sin^{-1}(v_s/v_r)$. Notably, this inclination angle slightly changes off the fault due to the velocity dispersion of viscoelastic materials, which has also been reported in laboratory experiments (Gori et al., 2018). In contrast to the

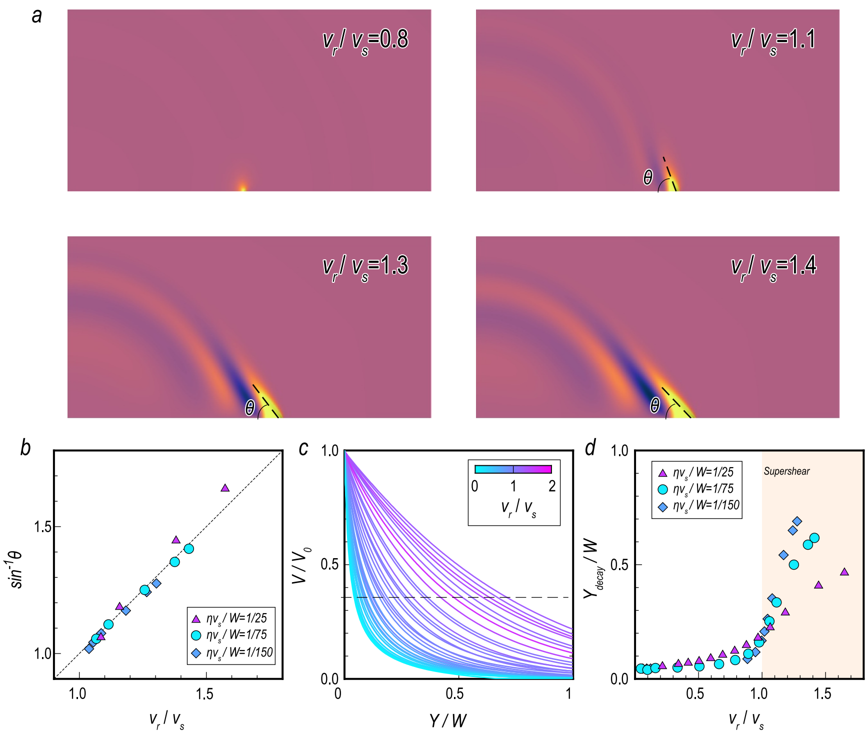

Figure 3. Mach fronts caused by supershear ruptures and their attenuation. (a) Snapshots of the velocity fields for four different rupture speeds (shown in the legend). θ indicates the Mach front angle in supershear ruptures. (b) The measured $\sin^{-1}(\theta)$ as a function of the normalized rupture speed v_r/v_s from the numerical simulations (symbols) are compared with the theoretical prediction (the dashed line). (c) Curves showing the relative amplitude of the velocity V/V_0 as a function of the normalized distance to the fault plane Y/W. V_0 is the amplitude of the velocity on the fault plane. The colors are coded according to the normalized rupture speed v_r/v_s. The dashed line marks the critical decay distance Y_{decay}/W at $V/V_0 = 1/e$. (d) Y_{decay}/W as a function of v_r/v_s for different values of $\eta v_s/W$ (in the legend).

Mach fronts caused by Mode II elastic ruptures whose amplitudes are undiminished with distance (Dunham, 2007; Dunham & Bhat, 2008), the amplitudes of Mach fronts in viscoelasticity decay exponentially with distance (Figure 3c). Y_{decay} is defined as the distance from the fault when the amplitude of the velocity decays to $1/e$ of the value on the fault. We find that Y_{decay}/W weakly increases with v_r/v_s in the subshear regime, while it dramatically increases in the supershear regime (Figure 3d). Additionally, Y_{decay}/W decreases as η increases, due to stronger viscoelastic dissipation. These results demonstrate that, on the one hand, viscoelasticity causes waves to propagate further by exciting Mach fronts, but on the other hand, the damping effects of viscoelasticity largely dissipate the energy of Mach fronts.

4. Theoretical Models

4.1. Basic Statement of the Problem

To derive the equation of energy balance, we consider a semi-infinite rupture propagating at a constant speed v_r along a shear-loading fault (Mode III) with a confined width W, embedded in a 3D infinite homogeneous isotropic medium. Linear elastic and Kelvin–Voigt viscoelastic materials are considered, respectively, with shear modulus, S-wave speed, and retardation time denoted as μ, v_s, and η. A Cartesian coordinate system (x, y, z) is adopted, where the rupture is confined to the $y = 0$ plane (the planar fault plane), and its strike and rupture propagation are parallel to the x direction. The displacement $u(x, y, z, t)$ is oriented along the z direction. For elongated ruptures, the displacement discontinuity is confined within $|z| < W/2$ on the planar fault plane, representing an infinitely long fault of finite width W (Figure 1a).

For simplicity, we consider a scalar wave equation that involves only S waves for a Mode III rupture:

$$\frac{\partial^2 u}{\partial x^2}+\frac{\partial^2 u}{\partial y^2}+\frac{\partial^2 u}{\partial z^2}=\frac{1}{v_s^2}\frac{\partial^2 u}{\partial t^2}. \tag{2}$$

Since the slip on a long fault with a uniform stress drop follows a semi-elliptical depth profile, the entire displacement field can be represented by a sinusoidal depth profile with a wavelength proportional to W, expressed as $u(x,y,t)e^{iz/(\gamma W)}$, where γ is a geometric coefficient. Thus, the 3D governing equation can be simplified to a 2.5D scalar equation (e.g., Lapusta, 2001; Lehner et al., 1981), which has been validated by 3D numerical simulations in elastic materials (Weng & Ampuero, 2019):

$$\frac{\partial^2 u}{\partial x^2}+\frac{\partial^2 u}{\partial y^2}-\frac{u}{(\gamma W)^2}=\frac{1}{v_s^2}\frac{\partial^2 u}{\partial t^2}, \tag{3}$$

where $\gamma = 1/\pi$ for the full-space model and $\gamma = 2/\pi$ for the half-space model, as derived theoretically (Weng & Ampuero, 2019, 2020). Equation 3 is known as the Klein–Gordon equation in physics. Considering a moving coordinate system $(\xi, y) = (x - v_r t, y)$, the time and spatial derivatives are related by $\partial/\partial t = (\partial/\partial\xi)\cdot(\partial\xi/\partial t) = -v_r\partial/\partial\xi$. Equation 3 can be transformed to the coordinates in the steady moving frame (ξ, y) as

$$\alpha_s^2\frac{\partial^2 u}{\partial \xi^2}+\frac{\partial^2 u}{\partial y^2}=k_w^2 u, \tag{4}$$

where $k_w = 1/(\gamma W)$ and $\alpha_s = \sqrt{1-(v_r/v_s)^2}$ is the Lorentz contraction factor. Due to the symmetry of the problem, we consider the solution in the half-space $y \geq 0$, with the boundary conditions at $y = 0^+$ given as follows:

$$\begin{aligned} \mu\frac{\partial u}{\partial y}\bigg|_{y=0^+} &= \begin{cases}\tau_+(\xi), & \text{if} \quad \xi > 0\\ \tau_f(\xi), & \text{if} \quad \xi < 0\end{cases}\\ u(\xi, 0^+) &= \begin{cases}0, & \text{if} \quad \xi > 0\\ u_-(\xi), & \text{if} \quad \xi < 0,\end{cases}\end{aligned} \tag{5}$$

where $\tau_f(\xi)$ is a given function for the shear stress on the ruptured fault segment, $\tau_+(\xi)$ is the undetermined shear stress ahead of the rupture tip, and $u_-(\xi)$ is the undetermined displacement on the ruptured fault segment (representing half of the displacement discontinuity on the fault).

For Kelvin–Voigt viscoelastic media, the 2.5D governing equation can be derived by replacing the shear modulus μ with the dynamic shear modulus $\mu\left(1+\eta\frac{\partial}{\partial t}\right)$:

$$\left(1+\eta\frac{\partial}{\partial t}\right)\left(\frac{\partial^2 u}{\partial x^2}+\frac{\partial^2 u}{\partial y^2}\right)-\frac{u}{(\gamma W)^2}=\frac{1}{v_s^2}\frac{\partial^2 u}{\partial t^2}, \tag{6}$$

where the properties of $\mu = \rho v_s^2$ is used, with ρ indicating the density, and the viscoelastic response in the z direction is ignored. The transformed equation in the steady moving frame becomes

$$-\eta v_r\frac{\partial^3 u}{\partial \xi^3}-\eta v_r\frac{\partial^3 u}{\partial \xi\partial y^2}+\alpha_s^2\frac{\partial^2 u}{\partial \xi^2}+\frac{\partial^2 u}{\partial y^2}=k_w^2 u, \tag{7}$$

where ηv_r has a length dimension. The boundary conditions at $y = 0^+$ are

$$
\begin{aligned}
\mu\left(1-\eta v_r\frac{\partial}{\partial\xi}\right)\frac{\partial u}{\partial y}\bigg|_{y=0^+} &= \begin{cases}\tau_+(\xi), & \text{if} \quad \xi>0\\ \tau_f(\xi), & \text{if} \quad \xi<0\end{cases}\\
u(\xi,0^+) &= \begin{cases}0, & \text{if} \quad \xi>0\\ u_-(\xi), & \text{if} \quad \xi<0.\end{cases}
\end{aligned}
\tag{8}
$$

The primary goal of the steady-state rupture problem is to analytically solve for the functions $\tau_+(\xi)$ and $u_-(\xi)$ given the function $\tau_f(\xi)$. The Wiener–Hopf method is a useful tool for this purpose, as introduced in Appendices A1 and A2, with additional details for the Wiener–Hopf method available in Barber et al. (1989), Freund (1998), Langer (1992), Lehner et al. (1981), and Willis (1967). Specifically, as Equation 6 is similar to the governing equations of cracks in 2D viscoelastic strips (Barber et al., 1989; Langer, 1992; Willis, 1967), some useful mathematical techniques from these papers can be readily applied to the viscoelastic problem in this study (see Appendix A2). Finally, based on the functions $\tau_+(\xi)$, $u_-(\xi)$, and $\tau_f(\xi)$ in the elastic and viscoelastic problems, the rupture-tip equations of motion are originally derived in this study.

4.2. Energy Balance for Elastic Ruptures

In this section, we derive the energy balance equation for an elastic rupture based on the given the function $\tau_f(x)$. Given a linear cohesive zone model, $\tau_f(x)$ is expressed as

$$
\tau_f(x) = \begin{cases}\tau_c\left(\dfrac{x}{\Lambda}+1\right), & \text{if} \quad -\Lambda<x<0\\ 0, & \text{if} \quad x<-\Lambda,\end{cases}
\tag{9}
$$

where τ_c is the dynamic strength drop and Λ is the cohesive zone size. Using the Wiener–Hopf technique (Appendix A1), the closed-form solution for the function $\tau_+(\xi)$ is:

$$
\tau_+(x) = \tau_\infty\left(\frac{e^{-\lambda x}}{\sqrt{\pi\lambda x}} + erf\sqrt{\lambda x}\right) - \frac{\tau_c}{\pi}\int_{-\Lambda}^{0}\frac{\sqrt{|\xi|}}{\sqrt{x}}\frac{(\xi/\Lambda+1)}{x+|\xi|}e^{-\lambda(x+|\xi|)}d\xi,
\tag{10}
$$

and the closed-form solution for the slip function, $u(x) = 2u_-(x)$, is given by:

$$
u(x) = \begin{cases}\dfrac{2\tau_\infty}{\mu\sqrt{k_w}}\displaystyle\int_0^{-x}\phi(\rho)d\rho - \dfrac{2\tau_c}{\mu\sqrt{\pi\alpha_s}}\displaystyle\int_0^{-x}\phi(\rho)d\rho\int_{-\Lambda}^{\rho+x}\dfrac{\left(\dfrac{\xi}{\Lambda}+1\right)e^{-\lambda(\rho-\xi+x)}}{\sqrt{\rho-\xi+x}}d\xi, & -\Lambda<x<0\\[2ex] \dfrac{2\tau_\infty}{\mu\sqrt{k_w}}\displaystyle\int_0^{-x}\phi(\rho)d\rho - \dfrac{2\tau_c}{\mu\sqrt{\pi\alpha_s}}\displaystyle\int_{-\Lambda-x}^{-x}\phi(\rho)d\rho\int_{-\Lambda}^{\rho+x}\dfrac{\left(\dfrac{\xi}{\Lambda}+1\right)e^{-\lambda(\rho-\xi+x)}}{\sqrt{\rho-\xi+x}}d\xi, & x<-\Lambda,\end{cases}
\tag{11}
$$

where $\lambda \equiv k_w/\alpha_s$, $\tau_\infty = \tau_+(\infty)$ is the static stress drop, and $\phi(\rho) = e^{-\lambda\rho}/\sqrt{\pi\alpha_s\rho}$ (details can be found in Appendix A1).

Considering the condition that the cohesive zone size is much smaller than the fault width, that is, $\lambda\Lambda \propto \Lambda/W \ll 1$, the singularity of shear stress at $x = 0^+$ can be canceled if letting

$$
\frac{\tau_\infty}{\tau_c} \simeq \frac{4\sqrt{\lambda\Lambda}}{3\sqrt{\pi}}.
\tag{12}
$$

The exact solution for Equation 12 can be derived by considering $\lim_{x\to 0^+} \tau_+(x)\sqrt{x} = 0$, whereas this does not provide additional physical insight. Normalizing all lengths in Equation 11 by setting $\tilde{\xi} = \xi/\Lambda$, $\tilde{x} = x/\Lambda$, and $\tilde{\rho} = \rho/\Lambda$ results in

$$u(\tilde{x}\Lambda) = \begin{cases} \dfrac{2\tau_\infty}{\mu k_w}\cdot\left[\sqrt{k_w}\,\Lambda\displaystyle\int_0^{-\tilde{x}}\phi(\tilde{\rho}\Lambda)\,d\tilde{\rho} - \dfrac{\tau_c k_w \Lambda^{3/2}}{\tau_\infty\sqrt{\pi\alpha_s}}\displaystyle\int_0^{-\tilde{x}}\phi(\tilde{\rho}\Lambda)\,I(\tilde{\rho}+\tilde{x})\,d\tilde{\rho}\right], -1<\tilde{x}<0 \\ \dfrac{2\tau_\infty}{\mu k_w}\cdot\left[\sqrt{k_w}\,\Lambda\displaystyle\int_0^{-\tilde{x}}\phi(\tilde{\rho}\Lambda)\,d\tilde{\rho} - \dfrac{\tau_c k_w \Lambda^{3/2}}{\tau_\infty\sqrt{\pi\alpha_s}}\displaystyle\int_{-\tilde{x}-1}^{-\tilde{x}}\phi(\tilde{\rho}\Lambda)\,I(\tilde{\rho}+\tilde{x})\,d\tilde{\rho}\right], \tilde{x}<-1, \end{cases} \tag{13}$$

where the function $I()$ is defined by

$$I(s) \equiv \int_{-1}^{s}\frac{(1+t)e^{-\lambda\Lambda(s-t)}}{\sqrt{s-t}}dt \simeq \frac{4}{3}(1+s)^{3/2}, \qquad \text{for} \quad s<0. \tag{14}$$

Note that the exponential term in the function $I(s)$ is dropped due to the assumption of $\lambda\Lambda \ll 1$. The slip rate can be derived from Equation 13 by taking $\dot{u}(x) = -v_r du/dx$. Therefore, the critical slip-weakening distance d_c can be derived from Equation 13 at $\tilde{x} = -1$

$$d_c = \frac{2\tau_\infty\Lambda}{\mu\sqrt{k_w}}\left[\int_0^1\phi(\tilde{\rho}\Lambda)\,d\tilde{\rho} - \frac{3}{4}\int_0^1\phi(\tilde{\rho}\Lambda)\,I(\tilde{\rho}-1)\,d\tilde{\rho}\right] \simeq \frac{3\tau_\infty\sqrt{\lambda\Lambda}}{\mu\sqrt{\pi}k_w}, \tag{15}$$

where Equation 12 is substituted. As $d_c \propto \sqrt{\lambda\Lambda} \propto \sqrt{\Lambda}/\sqrt{\alpha_s}$, this solution is physical only when α_s is positive, that is, $v_r < v_s$. Given a constant d_c, as v_r approaches v_s, λ approaches infinity, and ultimately, the dynamic cohesive zone size λ shrinks toward zero. The relation between the cohesive zone size Λ and v_r is analogous to the Lorentz length contraction that diminishes to zero as an object approaches the speed of light in the theory of relativity.

Combining Equations 12 and 15, the equation of energy balance is given by

$$G_0 \equiv \frac{\Delta\tau^2}{\mu k_w} = \frac{4}{9}\tau_c d_c \equiv G_c, \tag{16}$$

where $\Delta\tau = \tau_\infty$ and G_0 is independent of v_r. The form of G_0 in Equation 16 is exactly the same as that in Weng and Ampuero (2019), that is, ($G_0 = \frac{\Delta\tau^2 W}{\pi\mu}$ for the full-space model), except that the former uses the linear cohesive zone model, while the latter uses the singular model. In the linear cohesive zone model, the fault strength is assumed to be a linear function of the spatial distance between $x = -\Lambda$ and $x = 0$. As a result, the form of G_c in Equation 16 differs slightly from its definition in the linear slip-weakening friction $G_c = \frac{1}{2}\tau_c d_c$ used in the numerical simulations (Figure 4a), where the fault strength is a linear function of fault slip, rather than spatial fault distance.

The derivations of general forms of stress and slip in this study are consistent with the previous solution in Lehner et al. (1981) that considered a singular semi-infinite rupture model. Note that the energy balance equation for elastic ruptures, presented in Equation 16 and based on a cohesive zone model, was originally developed in this study and numerically validated.

4.3. Energy Balance for Viscoelastic Ruptures

In this section, we derive the energy balance equation for a viscoelastic rupture based on the same given function $\tau_f(x)$ in Equation 9. Using the Wiener–Hopf technique (Appendix A2), the closed-form solution for the function $\tau_+(\xi)$ is

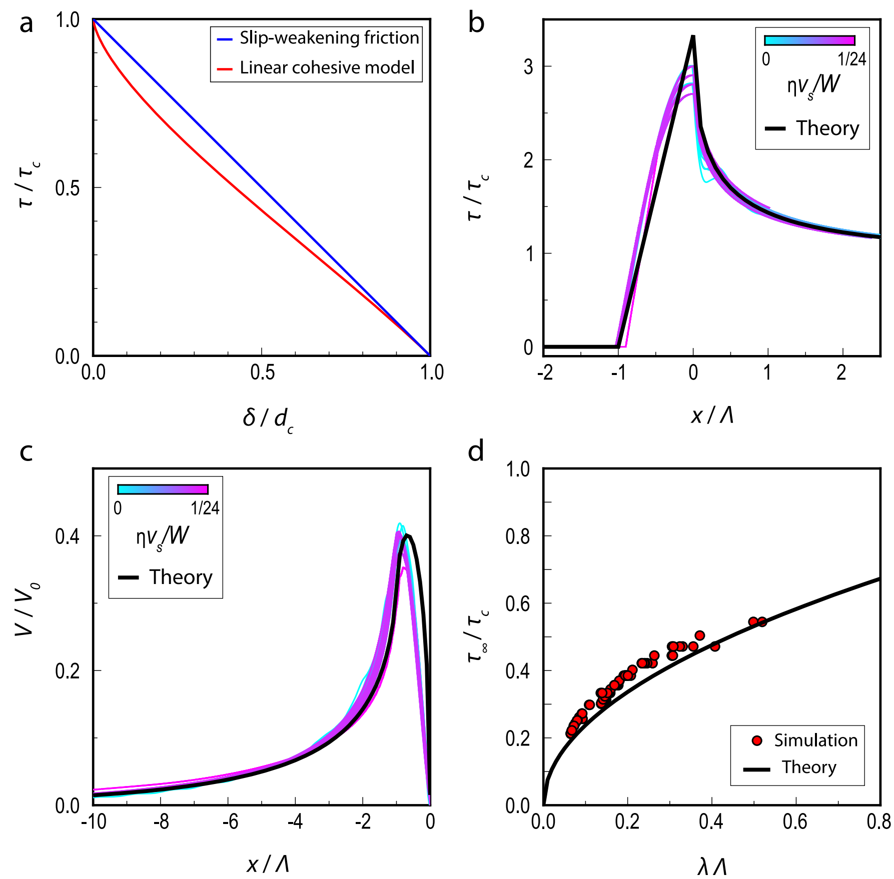

Figure 4. Detailed comparison between the simulations and the theory. (a) Normalized fault shear stress τ/τ_c evolves as a function of the normalized slip δ/d_c, where d_c is the critical slip-weakening distance and τ_c is the dynamic strength drop between the peak and residual strengths. (b–c) Normalized shear stress τ/τ_c (b) and fault slip rate V/V_0 (c) as a function of the normalized fault distance x/Λ, based on the 2.5D viscoelastic models with different G_c/G_0 and η (color-coded). The black curves represent predictions from fracture mechanics theory (Equations 17 and 18), where the integrals are numerically solved using Mathematica. V_0 is the characteristic slip rate derived from the theory, that is, $V_0 = (2v_r\tau_\infty)/(\mu k_w \Lambda)$. (d) The ratio of the static stress drop τ_∞ to the dynamic strength drop τ_c as a function of $\lambda\Lambda$, where λ is a theoretical parameter related to fault width and Λ is the size of the cohesive zone.

$$\tau_+(x) = \tau_\infty\left(\frac{e^{-\lambda_1 x}}{\sqrt{\pi\lambda_1 x}} + erf\sqrt{\lambda_1 x}\right) - \frac{\tau_c}{\pi}\int_{-\Lambda}^{0}\frac{\sqrt{|\xi|}}{\sqrt{x}}\,\frac{(\xi/\Lambda+1)}{x+|\xi|}e^{-\lambda_1(x+|\xi|)}d\xi, \tag{17}$$

and the closed-form solution for the slip function $u_-(x)$ is

$$u(\tilde{x}\Lambda) = \begin{cases} \dfrac{2\tau_\infty}{\mu\lambda_1}\cdot\dfrac{\Lambda}{\eta v_r}\displaystyle\int_0^{|\tilde{x}|} e^{\frac{\Lambda}{\eta v_r}\left(s-|\tilde{x}|\right)}\left[\sqrt{\lambda_1}\,\Lambda\int_0^{s}\phi(\tilde{p}\Lambda)\,d\tilde{p} - \frac{\tau_c\lambda_1\Lambda^{3/2}}{\tau_\infty\sqrt{\pi}}\int_0^{s}\phi(\tilde{p}\Lambda)\,I(\tilde{p}-s)\,d\tilde{p}\right]ds, & -1<\tilde{x}<0 \\ \dfrac{2\tau_\infty}{\mu\lambda_1}\cdot\dfrac{\Lambda}{\eta v_r}\displaystyle\int_0^{|\tilde{x}|} e^{\frac{\Lambda}{\eta v_r}\left(s-|\tilde{x}|\right)}\left[\sqrt{\lambda_1}\,\Lambda\int_0^{s}\phi(\tilde{p}\Lambda)\,d\tilde{p} - \frac{\tau_c\lambda_1\Lambda^{3/2}}{\tau_\infty\sqrt{\pi}}\int_{s-1}^{s}\phi(\tilde{p}\Lambda)\,I(\tilde{p}-s)\,d\tilde{p}\right]ds, & \tilde{x}<-1. \end{cases} \tag{18}$$

where the expressions of λ_1 and $\phi(x)$ depend on the range of rupture speed, as explained below.

The exact value of τ_c for canceling the singularity can be derived by taking $\lim_{x\to 0^+}\tau_+(x)\sqrt{x} = 0$. The asymptotic form, under the assumption that $\lambda_1\Lambda \ll 1$, is given by:

$$\frac{\tau_\infty}{\tau_c} \simeq \frac{4\sqrt{\lambda_1 \Lambda}}{3\sqrt{\pi}}. \tag{19}$$

The slip-weakening distance d_c can be derived from Equation 18 at $\tilde{x} = -1$

$$d_c = u(-\Lambda) = \frac{2\tau_\infty \Lambda}{\mu\sqrt{\lambda_1}} \int_0^1 \left(1 - e^{-\frac{\Lambda}{\eta v_r}\left(1-\tilde{\rho}\right)} - \frac{\Lambda}{\eta v_r}\int_0^{1-\tilde{\rho}} (t+\tilde{\rho})^{\frac{3}{2}} e^{-\frac{\Lambda}{\eta v_r}t} dt\right) \phi(\tilde{\rho}\Lambda)\, d\tilde{\rho}, \tag{20}$$

where Equation 19 is substituted.

The challenge in deriving the energy balance arises from the expressions for λ_1 and $\phi(x)$. To facilitate comparison with the simulation results, we assume the condition $\eta v_r \ll \Lambda$. For subshear rupture, λ_1 and $\phi(x)$ can be approximated as (Appendix A2)

$$\begin{aligned} \lambda_1 &\approx \left(\frac{k_w^2}{4\eta v_r}\right)^{\frac{1}{3}}, \\ \phi(x) &\approx e^{-2\lambda_1 x}/\sqrt{\eta v_r} \approx 1/\sqrt{\eta v_r}. \end{aligned} \tag{21}$$

Therefore, the rupture tip equation of motion for subshear ruptures is given by substituting Equation 21 into Equations 19 and 20

$$\frac{G_c}{G_0} \simeq \frac{2\sqrt{\pi}}{5}\left(\sqrt{\frac{\Lambda}{\eta v_r}} - \frac{5}{3}\sqrt{\frac{\eta v_r}{\Lambda}}\right) \cdot (4\eta v_r k_w)^{\frac{1}{3}}. \tag{22}$$

For supershear cases with $v_r > v_s$ and $\hat{\alpha}_s = \sqrt{(v_r/v_s)^2 - 1} \to 0$, λ_1 and $\phi(x)$ can be approximated as (Appendix A2)

$$\begin{aligned} \lambda_1 &\simeq \left(\frac{k_w^2}{\eta v_r}\right)^{\frac{1}{3}} + \frac{\hat{\alpha}_s^2}{\eta v_r} \\ \phi(x) &\approx e^{-\mathrm{Re}\{\lambda_2\}x}/\sqrt{\eta v_r} \approx 1/\sqrt{\eta v_r}. \end{aligned} \tag{23}$$

Therefore, the rupture tip equation of motion for supershear ruptures is given by substituting Equation 23 into Equations 19 and 20

$$\frac{G_c}{G_0} \simeq \frac{2\sqrt{\pi}}{5}\left(\sqrt{\frac{\Lambda}{\eta v_r}} - \frac{5}{3}\sqrt{\frac{\eta v_r}{\Lambda}}\right) \cdot \frac{\eta v_r k_w}{(\eta v_r k_w)^{\frac{2}{3}} + \hat{\alpha}_s^2}. \tag{24}$$

For fast supershear ruptures with $\hat{\alpha}_s \gg (\eta v_r k_w)^{\frac{1}{3}}$, Equation 24 asymptotically becomes

$$\begin{aligned} &\frac{G_c}{G_0} \simeq \frac{2\sqrt{\pi}}{5}\left(\sqrt{\frac{\Lambda}{\eta v_r}} - \frac{5}{3}\sqrt{\frac{\eta v_r}{\Lambda}}\right) \cdot \frac{\eta v_r k_w}{\hat{\alpha}_s^2} \\ \textbf{or} \quad &G_c \simeq \frac{2\sqrt{\pi}}{5}\frac{\Delta\tau^2\sqrt{\eta v_r \Lambda}}{\hat{\alpha}_s^2 \mu} \quad \textbf{when} \quad \eta v_r/\Lambda \ll 1. \end{aligned} \tag{25}$$

A key feature of fast supershear ruptures is that the dynamic energy release rate becomes independent of both rupture length and width. This implies that the 2.5D solution is also applicable to supershear ruptures in a 2D viscoelastic configuration. Because λ_1 is modulated by ηv_r rather than α_s, the solution can be physical even for $v_r > v_s$.

Specifically, for very low rupture speed $\alpha_s \simeq 1$, we have $\lambda_1 \simeq k_w$ and $\phi(x) \approx e^{-k_w x}/\sqrt{\pi x}$ (see Appendix A2). Thus, the critical slip-weakening distance d_c can be derived as

$$d_c \approx \frac{3\tau_\infty\sqrt{\Lambda}}{\mu\sqrt{\pi k_w}}\left(1 - \frac{\eta v_r}{\Lambda}\right). \tag{26}$$

Substituting Equation 19 into Equation 26, the equivalent fracture energy for slow ruptures can be written as

$$G_0 = G_{\text{equiv}} \approx G_c\left(1 + 2\frac{\eta v_r}{\Lambda}\right), \tag{27}$$

where a correction of a factor of 2 is made to fit the numerical results.

5. Numerical Results Predicted by the Theory

In Section 4, we extended the 3D theory of dynamic fracture mechanics to Kelvin–Voigt viscoelastic media and developed a new equation of motion for the rupture tip based on the principle of energy balance. Generally, the dynamics of viscoelastic ruptures depend on three nondimensional ratios: G_c/G_0, $\eta v_r/\Lambda$, and $\eta v_r/W$. The rupture tip equation of motion can be expressed in a general form as follows:

$$\frac{G_c}{G_0} \simeq \frac{2\sqrt{\pi}}{5}\cdot\left(\sqrt{\frac{\Lambda}{\eta v_r}} - \frac{5}{3}\sqrt{\frac{\eta v_r}{\Lambda}}\right)\cdot g\left(\frac{\eta v_r}{W}\right), \tag{28}$$

where the function $g\left(\frac{\eta v_r}{W}\right)$ has the asymptotic scaling relation, $g \sim (\eta v_r/W)^n$, and the coefficient n depends on the range of rupture speeds (refer to Equations 22, 24 and 25). Specifically, for slow ruptures, that is, $v_r \ll v_s$, the above equation of motion can be replaced by

$$G_0 \simeq G_c(1 + 2\eta v_r/\Lambda). \tag{29}$$

5.1. Full-Space Viscoelastic Numerical Models

We find that all supershear and subshear ruptures from the numerical simulations collapse onto a universal curve after normalization (represented by the symbols in Figure 5a), which is quantitatively predicted by Equation 28 (solid curve in Figures 5a and 6b). Equation 28 describe the complete form of the equation of motion, while an asymptotic form for the equation can be derived, which is $G_c/G_0/g \sim \sqrt{\frac{\Lambda}{\eta v_r}}$, when $\eta v_r/\Lambda \ll 1$. We find that this asymptotic form also serves as a good approximation for the predictions at small $\eta v_r/\Lambda < 0.2$ (dashed curves in Figure 5a). Additionally, the shear stress, slip rate on faults, and the dynamic cohesive zone size are also well predicted by fracture mechanics theory (Figures 4b and 4c).

Specifically, the new theory also predicts that v_r can be arbitrarily small, producing so-called slow earthquakes, as found by seismological observations (Bhattacharya & Viesca, 2019; Dragert et al., 2001). For slow ruptures, the viscoelasticity plays a role in damping the excess elastic energy, $G_0 - G_c$, to stabilize v_r at an arbitrarily low value. The equivalent fracture energy, incorporating frictional dissipation and viscous damping, can be expressed as $G_{equiv} \approx G_c(1 + 2\eta v_r/\Lambda)$, which well explains the energy balance of the simulated slow ruptures (Figure 5b). Previous studies (Fagereng & den Hartog, 2016; Wu, 2021; Barbot, 2019), which assumed viscous-frictional properties (where fault strength increases with the slip rate), have also produced slow ruptures in simulations as a mechanism for slow earthquakes. This study shows that slip-weakening faults embedded in viscoelastic media can likewise produce slow ruptures and that the viscous effect can be quantitatively incorporated into an equivalent frictional fracture energy G_{equiv} on the fault plane.

Viscoelastic ruptures can propagate at speeds exceeding the classical speed limit because the viscous dissipation term ηv_r serves as the leading coefficient (the coefficient of the highest-order derivative in the viscoelastic governing Equation 7), dominating the second leading coefficient, α_s. As a result, the size of the cohesive zone is physically modulated by ηv_r rather than by α_s, which serves as the leading coefficient in the elastic governing

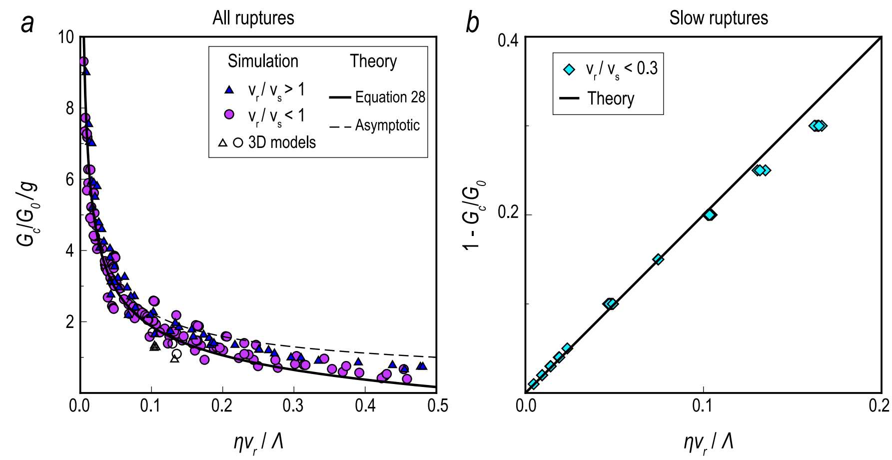

Figure 5. Rupture speeds predicted by theory. (a) Comparison between all the numerical results (symbols in the legend) and the theoretical predictions (curves in the legend). The vertical axis is the energy ratio between the fracture energy and the static energy release rate, G_c/G_0, divided by the universal function $g(\eta v_r/W)$, and the horizontal axis is the nondimensional ratio between the viscous dissipation distance and the cohesive length, $\eta v_r/\Lambda$. The solid and dashed curves indicate the theoretical predictions from Equation 28, with the solid curve representing the complete form and the dashed curve representing the asymptotic form assuming $\eta v_r/\Lambda \ll 1$. (b) Comparison between numerical results of slow ruptures (symbols in the legend) and theoretical prediction (line) in Equation 29.

Equation 4. Since ηv_r is usually smaller than the other length dimensions, Equation 28 can be simplified to an asymptotic form for subshear ruptures:

$$\frac{G_c}{G_0} \propto \left(\frac{\Lambda}{\eta v_r}\right)^{\frac{1}{2}} \left(\frac{\eta v_r}{W}\right)^{\frac{1}{3}}. \tag{30}$$

Equation 30 implies an asymptotic scaling relation $\Lambda^3 \sim \eta v_r$ given a constant G_c/G_0, which is consistent with the numerical results (Figure 6a). Our simulation results also demonstrate that Λ in viscoelastic materials is modulated by ηv_r rather than by α_s. For supershear ruptures, Equation 28 asymptotically becomes another form:

$$G_c \propto \frac{\Delta\tau^2 \sqrt{\eta v_r \Lambda}}{\hat{\alpha}_s^2 \mu}, \tag{31}$$

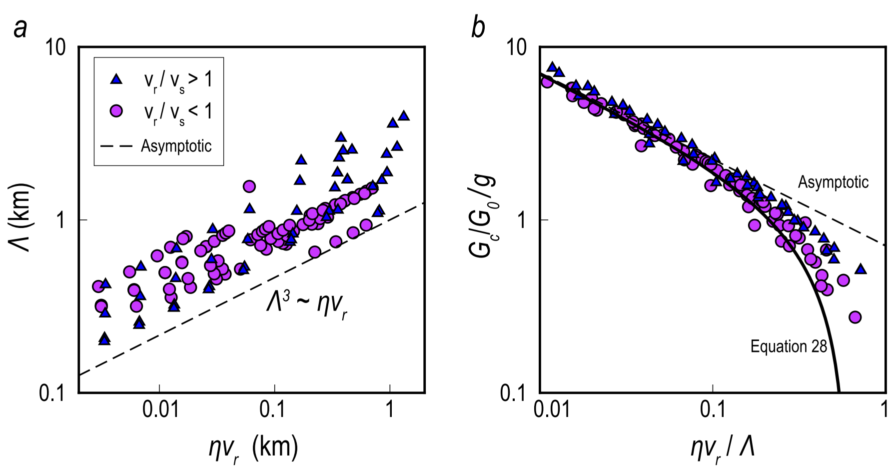

Figure 6. Scaling relations predicted by the theory. (a) The scaling relation between the size of the cohesive zone Λ and the viscous dissipation length ηv_r from the numerical simulations (symbols) is compared to the theoretical prediction (the dashed line). (b) The same as Figure 5a but in log-log plot.

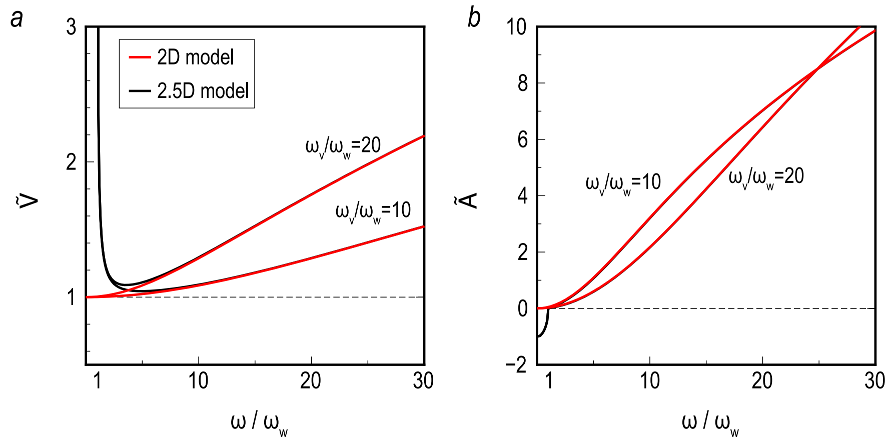

Figure 7. Analytical solution of the plane wave equation in viscoelastic materials. Normalized velocity dispersion (a) and attenuation (b) versus the normalized frequency ω/ω_w for the 2D and 2.5D viscoelastic models, where $\omega_w \equiv k_w v_s$ and $\omega_v \equiv 1/\eta$ are two characteristic frequencies that are related to the fault width and the viscoelastic retardation time.

where $\hat{\alpha}_s = \sqrt{(v_r/v_s)^2 - 1}$ does not produce any singularity at $v_r > v_s$. One important feature of supershear ruptures is that the dynamic energy release rate becomes independent of either rupture length or rupture width. Therefore, both the simulations and theory support that rupture propagation in viscoelasticity shall not be bounded by the classical speed limit.

While the complete solution of Equation 28 quantitatively predicts all rupture speeds, we can provide a complementary, qualitative explanation for the non-intuitive supershear ruptures: the local stiffening effect of Kelvin–Voigt viscoelasticity. We claim that the unbounded rupture speeds do not violate the law of cause and effect because the rupture speed in viscoelastic materials remains below the wave speed locally around the rupture tip, which is elevated due to the velocity dispersion of viscoelasticity at high frequency (Figure 7a; Appendix A3). Because the attenuation also remarkably increases at high frequency (Figure 7b), the stiffening effect in viscoelasticity is confined to be local. This local effect of viscoelasticity is similar to that of locally stiffening hyperelasticity (Gumbsch & Gao, 1999) on supersonic cracks, except that the former is strain rate dependent and the latter is strain dependent. While local viscoelastic stiffening has been reported in PMMA experiments (Gori et al., 2018), it remains to be validated whether this effect is prevalent in PMMA and other materials, such as natural rocks. Due to the local stiffening effect in viscoelasticity, the energy balance of supershear ruptures is dominated by the local properties around the tips (Equation 31) rather than by the macroscopic lengths of the model configuration. To validate this, we conducted additional 2D numerical simulations, assuming that the fault width W is infinite. We find that, for low shear loading, the rupture in 2D asymptotically approaches v_s while the rupture in 2.5D acquires a steady-state value lower than v_s (Figure 8), which means the fault width plays a significant role in subshear ruptures. Whereas for high shear loading, rupture speeds and peak slip rates in 2.5D and 2D converge and the ruptures are steady state (Figure 8), which implies that the energy balance of supershear ruptures is independent of either rupture length or rupture width and is controlled only by the local properties in Equation 31. These results show that Equation 31 is also applicable to supershear ruptures in a 2D viscoelastic configuration; nevertheless, it requires a quantitative comparison with laboratory experiments (Gori et al., 2018).

5.2. Finite Thickness of the Viscoelastic Layer

The elasticity of both natural rocks (Q. B. Zhang & Zhao, 2013; Fan et al., 2011; Yan et al., 2022) and polymers (Mai et al., 2020) varies according to the state of deformation: exhibiting linear elasticity under small and/or slow deformations, and transitioning to inelasticity under large and/or rapid deformations. Seismological (H. Zhang et al., 2023) and geological (Fagereng & Beall, 2021) observations reveal that damaged zones, where viscous deformation is more likely to occur, are highly confined to seismogenic faults that host historical earthquakes. To investigate the applicability of the viscoelastic theory, we simulate dynamic rupture models featuring a viscoelastic layer of finite thickness H embedded within a full-space elastic medium (Figure 9a) to mimic the observed damage fault zones surrounded by linear elastic materials. We find that there are two end-member behaviors at

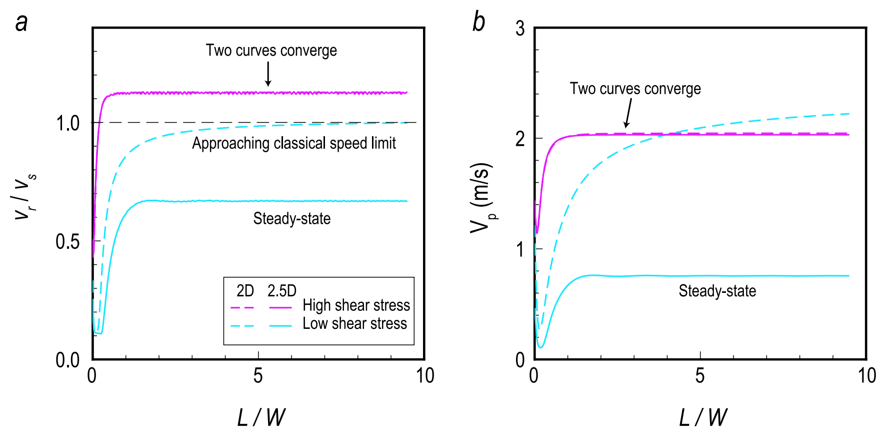

Figure 8. Comparison between the 2D and 2.5D viscoelastic models. (a) Normalized rupture speeds v_r/v_s as a function of the normalized distance L/W, based on the 2D and 2.5D viscoelastic models with different shear stress loadings (as indicated in the legend). (b) Peak slip rate V_p on fault as a function of the normalized distance L/W from the same models in (a). Rupture speed and peak slip rate in 2D and 2.5D converge in the supershear regime.

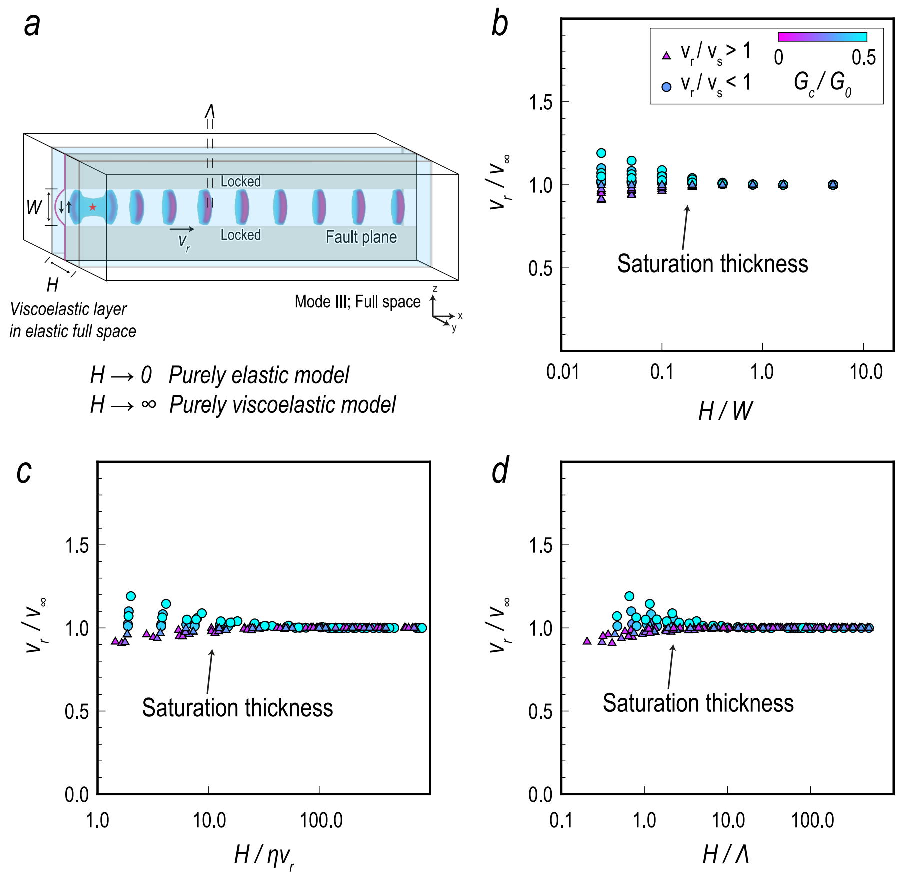

Figure 9. Effects of the thickness of the viscoelastic layer. (a) Schematic outline of the geometry of the viscoelastic layer. Outside the viscoelastic layer, the material is linearly elastic. The small arrows show the direction of homogeneous shear loading. (b–d) Normalized terminal speed v_r/v_∞ (symbols in the legend) versus three length ratios: H/W, $H/\eta v_r$, and H/Λ, where v_∞ is the terminal speed when $H \rightarrow \infty$. There is a critical thickness above which the terminal speed becomes independent of H. The colors are coded according to the energy ratio G_c/G_0.

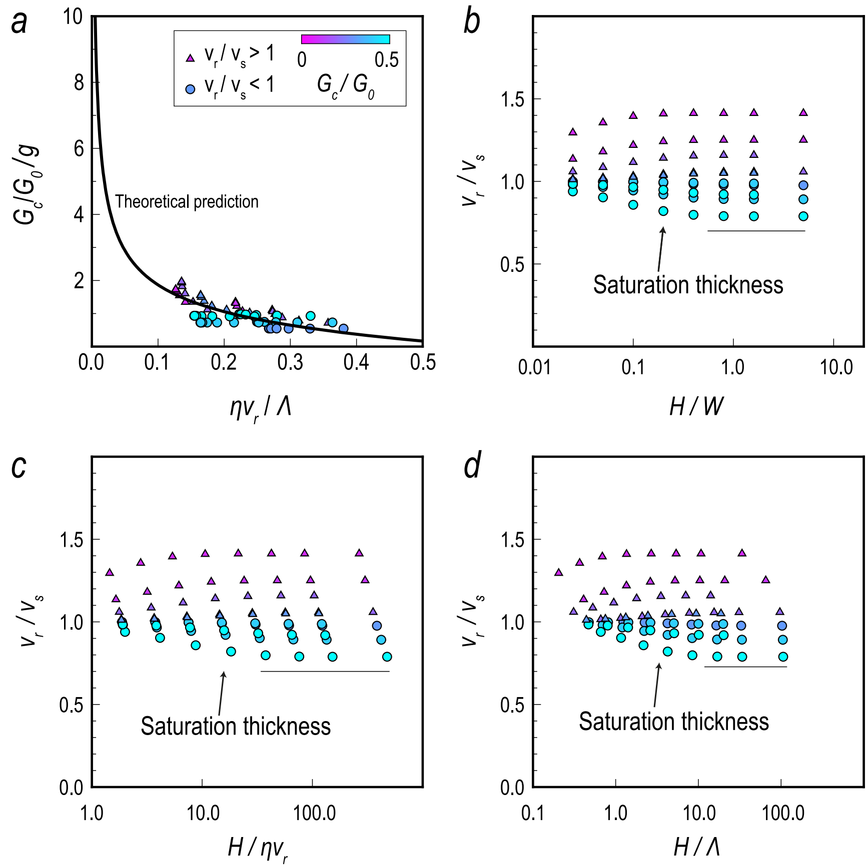

Figure 10. Effects of the thickness of the viscoelastic layer. (a) Comparison between the numerical simulations of different H (symbols in the legend) and the theoretical prediction (black curve). The black curve indicates the theoretical prediction from Equation 28. (b–d) Normalized terminal speed v_r/v_s versus the ratios of H/W (b), $H/\eta v_r$ (c), and H/Λ (d) for the same models shown in (a). There is a critical thickness above which the terminal speed becomes independent of H. The colors are coded according to the energy ratio G_c/G_0.

small and large H (Figures 9 and 10). As H approaches zero, the viscoelastic solution converges to the elastic solution, causing the rupture speeds to asymptotically approach the limiting speed. For non-zero H, ruptures attain a steady-state terminal speed that is slower than the limiting speed. As H increases, the steady-state speed approaches the full-space viscoelastic solution once a critical nondimensional thickness is exceeded, such as $H/W > 0.1$, $H/\eta v_r > 10$, or $H/\Lambda > 1$. In addition, we find that the theoretical Equation 28 remains applicable for explaining the numerical results at finite H (Figure 10a), although discrepancies are anticipated as H approaches zero. Our numerical results further indicate that even the smallest tested H (twice the size of the model grids) can yield steady-state ruptures with terminal speeds either greater or less than v_s (Figure 11).

The length scales of damaged fault zones (Huang et al., 2014) are typically on the order of $H \sim 0.1{-}1$ km. The typical seismogenic widths of strike-slip faults are $W \sim 10{-}20$ km, leading to a ratio of $H/W \sim 0.01{-}0.1$ within the tested range of parameters in this study. In addition, laboratory experiments have also shown that materials such as PMMA, elastomers, and polyacrylamide gels exhibit viscoelastic properties (Gori et al., 2018; Mai et al., 2020; Wang et al., 2023), with viscoelasticity potentially being confined to a thin layer due to locally elevated temperatures. Given that viscoelasticity is a common feature in both geological rocks and engineering materials, its effects on dynamic fracture mechanics should be considered, even when its geometrical length is significantly shorter than other fault dimensions.

6. Discussion

Despite the simplifying assumptions of the Kelvin–Voigt viscoelastic model used in this study, which have limitations at the higher end of the frequency spectrum, the model represents a significant advancement in

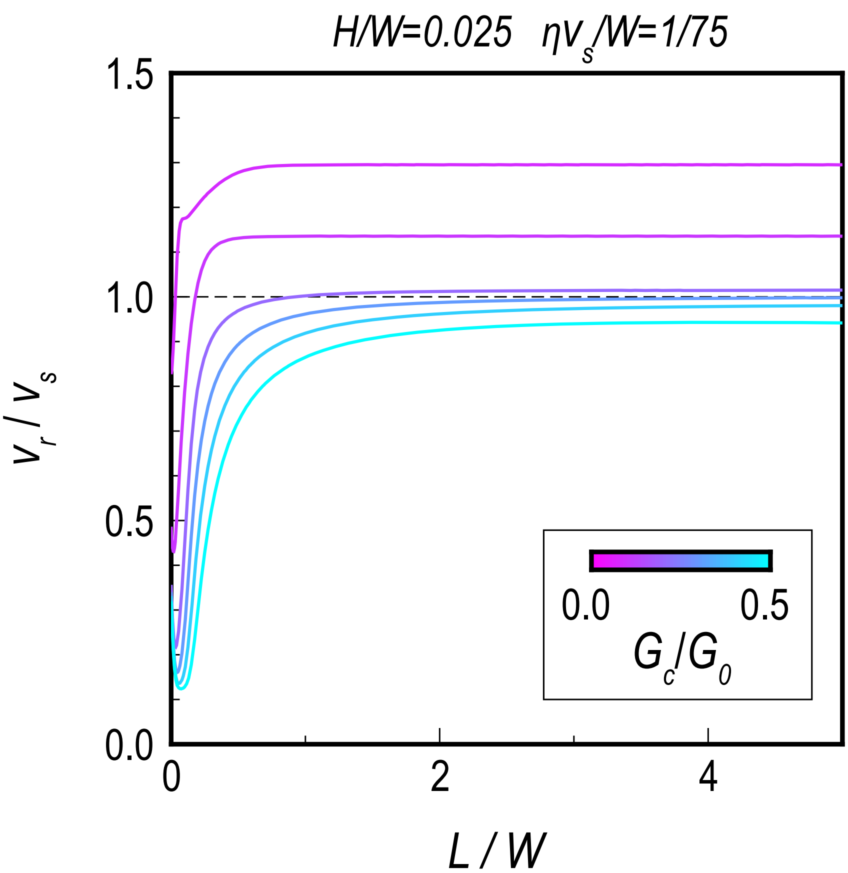

Figure 11. Narrow viscoelastic layer can break the speed limit. Normalized rupture speed v_r/v_s as a function of the normalized rupture distance L/W from the 2.5D models with the smallest thickness of the viscoelastic layer in the simulations, that is, $H/W = 0.025$. The colored curves are coded by the energy ratio G_c/G_0.

integrating analytical and numerical results. Future work could extend the Kelvin–Voigt model to more complex frameworks, such as the standard linear solids (Robertsson et al., 1994), which retains the physically valid properties of the Kelvin–Voigt model while also exhibiting meaningful behavior in the high-frequency regime. Additionally, further research is needed to account for the reduced rigidity of pre-existing damage zones, as observed in real fault environments (e.g., Huang et al., 2014), as well as co-seismic damages that interact with rupture propagation (e.g., Andrews, 2005), where the reduced S-wave speed may compete with the viscoelasticity in controlling rupture speeds.

We simulated several 3D models for a quantitative comparison with the 2.5D models. We find that both the 2.5D and 3D models reach steady-state terminal speeds around $L/W = 3$ (Figure 12a), while supershear ruptures reach steady-state speeds around $L/W = 1$ (Figure 12b). Although the supershear ruptures in 3D are slightly lower than those in 2.5D, the terminal speeds from both models are quantitatively consistent with the theoretical prediction (Figure 12c). The difference in the supershear speed regime can be explained by the different geometrical attenuations of shock waves in 3D and 2.5D, noting that the 2.5D model ignores the viscoelastic response in the vertical direction. We confirm that the 2.5D simulations and theoretical prediction can well approximate the 3D effects of finite rupture depth in viscoelastic materials, particularly for subshear ruptures.

This work primarily focuses on the fundamental principles of viscoelastic ruptures by relating non-dimensional forms of quantities: G_c/G_0, $\eta v_r/\Lambda$, and $\eta v_r/W$. Theoretically, this fundamental theory enables the estimation of rupture speeds using the measured values of the retardation time η obtained from geological or engineering materials, provided that other parameters can be constrained. Directly constraining η for fault damage zones is challenging; however, it can be indirectly estimated through seismological observations. In seismology, the Q-value is commonly used to quantity the seismic attenuation, defined by

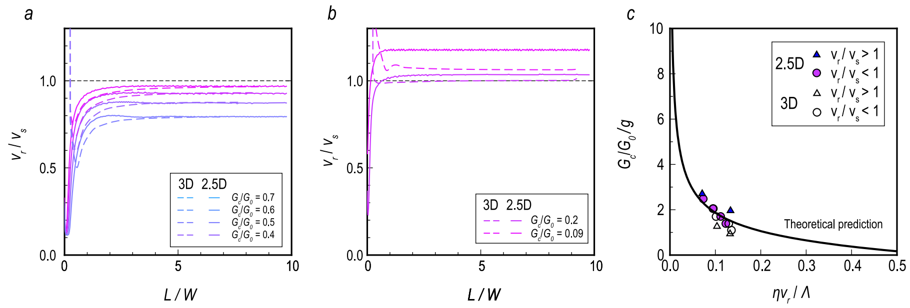

Figure 12. Comparison between the 3D and 2.5D viscoelastic models. (a–b) Normalized rupture speeds v_r/v_s as a function of the normalized distance L/W from the 3D and 2.5D viscoelastic models with different G_c/G_0 (in the legend). Note that the differences between the dashed and solid curves at $L/W < 1$ are due to the slightly different nucleation conditions in the 2.5D and 3D models, which do not affect the terminal speeds. (c) Comparison between the 3D and 2.5D numerical results (symbols in legend) and the theoretical prediction (black curve).

$$Q^{-1}(\omega) = -\frac{\Delta E}{2\pi E}, \tag{32}$$

where $\omega = 2\pi f$ represents the frequency of seismic waves, E is the peak strain energy and $-\Delta E$ is the energy loss per cycle. In viscoelastic materials, planar waves take the general Fourier form $U(\omega) = U_0 e^{-A(\omega)x - iB(\omega)x}$ (for the specific forms of $A(\omega)$ and $B(\omega)$, refer to Appendix A3). If we only consider the case where $Q \gg 1$, then the Q-value can be expressed as

$$Q^{-1}(\omega) = \frac{2v_s}{\omega} \cdot A(\omega) = \sqrt{\frac{2}{\sqrt{1+(\eta\omega)^2}} - \frac{2}{1+(\eta\omega)^2}}, \tag{33}$$

where $Q^{-1}(\omega) \approx \eta\omega$ is approximated if $\eta\omega \ll 1$. The seismologically measured Q-value for fault damage zones is roughly ~ 40 (e.g., Ben-Zion, 1998; H. Zhang et al., 2023), which results in a retardation time for fault damage zones of $\eta \approx 1/(2\pi f Q) \approx 0.004\ s$, assuming the seismic signal frequency of $f = 1Hz$. Given typical values of $v_s \sim 3000$ m/s and $W \sim 10$ km for a large crustal earthquake, $\eta v_s \sim 10$ m and $\eta v_s/W$ is on the order of 1/1,000, which falls within the tested range of numerical simulations in this study. Since the seismologically measured Q-value is only valid within a specific frequency range, it is challenging to determine which stress-strain constitutive model is most appropriate for the fault damage zone. In the theoretical relation of Equation 28, G_0 and W can be estimated through geodetic observations, while constraining the other quantities, G_c and Λ, remains challenging. Specifically, the theoretical Equation A31 for slow ruptures enables the estimation of terminal rupture speeds based on measurements of the critical slip-weakening distance d_c, the dynamic cohesive zone size Λ, and the stress drop $\Delta\tau$. In the future, implementing strain meters across the fault segments where slow slips and/or shallow earthquakes occur may provide a direct constraint on these parameters, such as fiber-optic distributed strain sensing.

For slow ruptures, rupture speeds can be estimated based on a simple energy balance equation, $G_0/G_c = 1 + 2\eta v_r/\Lambda$. Since the radiation energy of slow ruptures is negligible, all released elastic energy (G_0) will be dissipated through friction (G_c) and viscous damping (G_v), that is, $G_0 = G_c + G_v$. Considering that the viscous damping at slow speeds can be formalized for different slip directions, we propose that this energy balance equation can be extended to Modes I and II by adjusting the coefficients accordingly:

$$\frac{G_v}{G_c} = C \cdot \frac{\eta v_r}{\Lambda}, \tag{34}$$

where C is a geometrical coefficient on the order of 1 (e.g., $C = 2$ in Mode III), and G_v/G_0 represent the amount of energy dissipated through viscosity to the energy dissipated through friction. An interesting aspect of this energy balance is that the ratio of energies has a linear relationship with the ratio of lengths. Since the elastic ruptures have the scaling relations of $G_c \propto \Delta\tau^2 W$ and $G_c \propto \tau_c^2 \Lambda$ (Equation 12), the viscoelastic ruptures have a scaling relation of $G_v \propto \tau_v^2 \eta v_r$, where $\tau_v = \sqrt{C}\tau_c$ represents the stress response of viscoelasticity based on Equation 34. Therefore, we suggest that Equation 34 might provide a fundamental framework in understanding the propagation of slow earthquakes in other viscoelastic models (Beall et al., 2019; Behr & Bürgmann, 2021; Behr et al., 2018, 2021; Lavier et al., 2021; Ujiie et al., 2018), where an equivalent η of units of time can be derived, which is worthy to investigate in the future.

A compilation of rupture speeds for global SSEs and regular earthquakes (Weng & Ampuero, 2022, and the references therein) shows a gap in rupture speeds between ~ 10 m/s and ~ 1000 m/s. Given a value of $v_s \sim 3330$ m/s, leading to a speed gap of $0.003 < v_r/v_s < 0.3$. Our theoretical prediction for slow ruptures (Equation 34) is expected to be applicable over a continuous range of speeds. If the observed speed gap is caused by the mechanics, then natural faults should satisfy the condition: $\frac{G_v}{G_c} = \frac{2\eta v_s}{\Lambda} \cdot \frac{v_r}{v_s} < 0.006\,\frac{\eta v_s}{\Lambda}$. Given empirical values of $\Lambda \sim 100\,\text{m} - 1000\,\text{m}$ and $\eta \sim 0.004$ s, the critical condition for the observed "fastest" SSEs (i.e., $v_r \sim 10$ m/s) is $G_v/G_c \sim 10^{-3} - 10^{-4}$. The upper bound of rupture speed for currently observed SSEs might be due to relatively lower viscous dissipation compared to frictional dissipation, that is, $G_v/G_c \ll 10^{-3} - 10^{-4}$. The dimensionless analysis suggests that the absolute value of $G_v = G_0 - G_c$ related to inelastic dissipation in natural rocks is expected to be much smaller than G_c, the frictional resistance at the fault interface during SSEs.

The fracture mechanics theory and simulations in this study are based on the assumption of a single pre-existing fault. Thus, rupture dynamics are physically governed by the interaction between frictional behavior on faults and wave propagation in materials. Frictional behavior on faults has been modeled using either slip-dependent friction, such as the slip-weakening friction laws as used in this study, or slip-rate-dependent friction laws (Dieterich, 1979; Rubin & Ampuero, 2005; Ruina, 1983), both of which simulate dynamic rupture propagation with a finite cohesive zone. To model wave propagation in materials, linear elastic models are most commonly used, exhibiting a constant wave propagation speed that is independent of strain. Non-linear elastic models, such as hyperelastic materials (e.g., Gumbsch & Gao, 1999), allow wave propagation speed to vary with strain, but their deformation remains fully reversible. In contrast to elastic materials, inelastic materials are generally not fully reversible upon the removal of applied stress, and their wave propagation speed depends on the rate of strain, as shown in viscoelastic materials (Figure 7a), and also on the yielding stress, as described in continuum damage rheology of viscoplastic materials (Ben-Zion & Lyakhovsky, 2019; Jara et al., 2021; Lyakhovsky et al., 2005). Some studies (Wu, 2021) have simplified the complex stress-strain relations in hosting materials by an equivalent, simple frictional formulation on the faults to simulate slow ruptures. In practice, any combination of frictional and material models can be employed for specific rupture problems with pre-existing faults. If the assumption of pre-existing faults is relaxed, rupture simulations can be conducted by considering the granular flow in fault damage zones (Gao et al., 2018; Åström et al., 2000); however, whether the developed equations of motion remain valid requires further investigation.

7. Conclusion

In fracture mechanics theories based on linear elasticity, rupture propagation is governed solely by the ratio of fracture energy to energy release rate, with rupture speeds bounded by the classical speed limit. In contrast, the new theory incorporating Kelvin–Voigt viscoelasticity—a common feature in many materials—adds two additional ratios of characteristic lengths, which thus allow for both unbounded rupture speeds and arbitrarily low speeds. Particularly in the supershear regime, the energy balance becomes independent of any macroscopic scale and is dictated solely by local properties around the rupture tip, indicating that the theoretical predictions for 2D and 3D supershear ruptures are energetically similar. These findings provide a quantitative framework for understanding rupture propagation in viscoelastic materials through the concept of energy balance, fundamentally advancing our understanding of fracture mechanics.

Appendix A

A1. Wiener–Hopf Technique for Elastic Problem

Here, we determine $\tau_+(\xi)$ and $u_-(\xi)$ using the governing equation (Equation 4) and boundary conditions (Equation 5) applicable to elastic materials. Applying the two-sided Laplace transform to Equation 4 yields

$$\frac{\partial^2 U}{\partial y^2} = \left(k_w^2 - \alpha_s^2 \zeta^2\right) U, \tag{A1}$$

and the general solution is

$$U(\zeta, y) = P(\zeta) e^{-\beta y}, \quad \beta = \sqrt{k_w^2 - \alpha_s^2 \zeta^2}, \tag{A2}$$

where $P(\zeta)$ is an undetermined function. Note that the other term $e^{\beta y}$ is not considered in the above solution due to the condition $\partial u/\partial \xi, \partial u/\partial y \rightarrow 0$ when $\xi^2 + y^2 \rightarrow \infty$. Applying the same Laplace transform to the boundary condition (Equation 5) and substituting Equation A2 yield

$$\begin{aligned} -\mu\beta U_- &= T_+ + T_- \\ T_- &= \int_{-\infty}^{0} \tau_f(\xi) e^{-\zeta\xi} d\xi, \end{aligned} \tag{A3}$$

where T_+ and U_- are the Laplace transforms of τ_+ and u_-, respectively. The term $K(\zeta) \equiv 1/\beta$ is defined, leading to the properties of $K(0) \sim 1/k_w$ and $K(\infty) \sim 1/(i\alpha_s\zeta)$. Using the Wiener–Hopf technique, the function $K(\zeta)$ can be decomposed by inspection (Freund, 1998; Lehner et al., 1981)

$$K(\zeta) = K_+(\zeta) K_-(\zeta), \tag{A4}$$

$$\begin{aligned} K_+(\zeta) &= 1/\sqrt{k_w + \alpha_s \zeta} \\ K_-(\zeta) &= 1/\sqrt{k_w - \alpha_s \zeta}, \end{aligned} \tag{A5}$$

where the branch points are $\zeta = \pm\lambda \equiv \pm k_w/\alpha_s$ and the branch cuts of $K_+(\zeta)$ and $K_-(\zeta)$ are introduced along $\zeta < -\lambda$ and $\zeta > \lambda$, respectively. As $T_-(\zeta)$ and $U_-(\zeta)$ are analytic in $\mathrm{Re}\{\zeta\} < 0$ and $T_+(\zeta)$ is analytic in $\mathrm{Re}\{\zeta\} > -\lambda$, Equation A3 is expected to be analytic in the strip $-\lambda < \mathrm{Re}\{\zeta\} < 0$. The goal of the following decompositions is to make the left side of Equation A3 being analytic in $\mathrm{Re}\{\zeta\} < 0$ and the right side of Equation A3 be analytic in $\mathrm{Re}\{\zeta\} > -\lambda$. The first decomposition results in the following form

$$-\mu \frac{U_-(\zeta)}{K_-(\zeta)} = K_+(\zeta) T_+(\zeta) + K_+(\zeta) T_-(\zeta). \tag{A6}$$

According to the final value theorem at the limit of $\zeta \rightarrow 0$, $-\zeta U_-(\zeta) = u(-\infty) = u_{-\infty}$, $\zeta T_+(\zeta) = \tau(\infty) = \tau_\infty$, and $-\zeta T_-(\zeta) = \tau(-\infty) = \tau_{-\infty}$. Equation A6 implies $\mu u_{-\infty}/K_-(0) = K_+(0)(\tau_\infty - \tau_{-\infty})$, where $\Delta\tau = \tau_\infty - \tau_{-\infty}$ is the static stress drop. This study uses the convention that $\tau_f(-\infty) = 0$, so $\tau_{-\infty} = 0$ and $\Delta\tau = \tau_\infty$. The second term on the right side of Equation A6 can be further decomposed by means of Cauchy's theorem

$$K_+(\zeta) T_-(\zeta) = F_+(\zeta) + F_-(\zeta), \tag{A7}$$

where

$$F_\pm(\zeta) = \mp \frac{1}{2\pi i} \int_{C_\pm} \frac{K_+(\zeta') T_-(\zeta')}{\zeta' - \zeta} d\zeta'. \tag{A8}$$

here C_+ and C_- are contours from $-i\infty$ to $i\infty$, through the left and right of the pole at $\zeta' = \zeta$, respectively, and ζ is the chosen location within the analytic strip $-\lambda < \mathrm{Re}\{\zeta\} < 0$. After decomposition, Equation A6 can be written as

$$-\mu\zeta\frac{U_-(\zeta)}{K_-(\zeta)} - \zeta F_-(\zeta) = \zeta K_+(\zeta)T_+(\zeta) + \zeta F_+(\zeta), \tag{A9}$$

where both sides are multiplied with ζ to make the limits at $\zeta \to 0$ being finite. Therefore, the left side of Equation A9 is analytic in $\mathrm{Re}\{\zeta\} < 0$ and the right side of Equation A9 is analytic in $\mathrm{Re}\{\zeta\} > -\lambda$. According to Liouville's theorem, both sides of Equation A9 must be equal to a constant, which is determined to be $\tau_\infty K_+(0)$ at $\zeta = 0$. The solution can be written as

$$\begin{aligned} T_+(\zeta) &= \frac{\tau_\infty K_+(0)}{\zeta K_+(\zeta)} - \frac{F_+(\zeta)}{K_+(\zeta)} \\ U_-(\zeta) &= -\frac{\tau_\infty K_+(0)K_-(\zeta)}{\mu\zeta} - \frac{F_-(\zeta)K_-(\zeta)}{\mu}. \end{aligned} \tag{A10}$$

The next step is to invert T_+ and U_-. The formal inversions of Laplace transform for T_+ and U_- are as follows:

$$\begin{aligned} \tau_+(x) &= \frac{1}{2\pi i}\int_{\epsilon-i\infty}^{\epsilon+i\infty}\left[\frac{\tau_\infty K_+(0)}{\zeta K_+(\zeta)} - \frac{F_+(\zeta)}{K_+(\zeta)}\right]e^{\zeta x}d\zeta \qquad \text{for} \quad x > 0 \\ u_-(x) &= \frac{1}{2\pi i}\int_{\epsilon-i\infty}^{\epsilon+i\infty}\left[-\frac{\tau_\infty K_+(0)K_-(\zeta)}{\mu\zeta} - \frac{F_-(\zeta)K_-(\zeta)}{\mu}\right]e^{\zeta x}d\zeta \qquad \text{for} \quad x < 0, \end{aligned} \tag{A11}$$

where ϵ is a real number in the interval $-\lambda < \epsilon < 0$. The detailed evaluations of these two equations are lengthy and are presented in Appendix A4, where the results can be summarized as follows:

$$\tau_+(x) = \tau_\infty + \frac{\tau_\infty}{2\sqrt{\pi\lambda}}\int_x^\infty \frac{e^{-\lambda\xi}}{\xi^{3/2}}d\xi - \frac{1}{\pi}\int_{-\infty}^0 \frac{\sqrt{|\xi|}}{\sqrt{x}}\frac{1}{x+|\xi|}e^{-\lambda(x+|\xi|)}\tau_f(\xi)d\xi, \tag{A12}$$

$$u_-(x) = \frac{\tau_\infty}{\mu\sqrt{k_w}}\int_0^{-x}\phi(\rho)d\rho - \frac{1}{\mu\sqrt{\pi\alpha_s}}\int_0^{-x}\phi(\rho)d\rho\int_{-\infty}^{\rho+x}\frac{e^{-\lambda(\rho-\xi+x)}}{\sqrt{\rho-\xi+x}}\tau_f(\xi)d\xi, \tag{A13}$$

where

$$\phi(\rho) = \frac{1}{2\pi i}\int_{\delta-i\infty}^{\delta+i\infty} e^{-\zeta\rho}K_-(\zeta)d\zeta \qquad \text{for} \quad \rho > 0. \tag{A14}$$

$\phi(\rho) = 0$ for $\rho < 0$ because all singularities in $K_-(\zeta)$ lie in the right half plane $\mathrm{Re}\{\zeta\} > 0$. The fault slip $u(x)$ is twice the displacement discontinuity $u_-(x)$ on $y = 0$, that is, $u(x) = 2u_-(x)$. Equations A12 and A13 are consistent with the general solution in Lehner et al. (1981).

A2. Wiener–Hopf Technique for Viscoelastic Problem

Here, we determine $\tau_+(\xi)$ and $u_-(\xi)$ using the governing equation (Equation 7) and boundary conditions (Equation 8) applicable to viscoelastic materials. Applying the two-sided Laplace transform to Equation 7 yields

$$\frac{\partial^2 U}{\partial y^2} = \frac{\eta v_r\zeta^3 - \alpha_s^2\zeta^2 + k_w^2}{1-\eta v_r\zeta}U. \tag{A15}$$

The general solution for the above equation is

$$U(\zeta, y) = P(\zeta)e^{-\beta(\zeta)y}; \quad \beta(\zeta) = \sqrt{\frac{(\lambda_1+\zeta)(\lambda_2-\zeta)(\lambda_3-\zeta)}{1/\eta v_r - \zeta}}, \tag{A16}$$

where λ_i are the three solutions of the cubic equation $\eta v_r \zeta^3 - \alpha_s^2 \zeta^2 + k_w^2 = 0$. Analysis of this cubic equation shows that if $\eta v_r k_w < \frac{2\alpha_s^3}{3\sqrt{3}}$ there are three real roots (one negative number and two positive numbers), otherwise there are one negative real root and two complex roots with positive real parts. Due to this structure, λ_1 is defined as a positive real number and thus $-\lambda_1$ represents the negative real root of the cubic equation. Since $K(\zeta) \equiv 1/\beta$ is defined, $K(0) \sim 1/k_w$ and $K(\infty) = 1/(i\zeta)$, where one property of the cubic function is used. Applying the same Laplace transform to the boundary condition (Equation 8) and substituting Equation A16 yield

$$\begin{aligned} -\mu\beta \cdot [(1-\eta v_r \zeta)\, U_-] &= T_+ + T_- \\ T_- &= \int_{-\infty}^{0} \tau_f(\xi) e^{-\zeta\xi} d\xi. \end{aligned} \tag{A17}$$

Similar to the technique used in the elastic model, the solution in viscoelastic media is derived as

$$\begin{aligned} T_+(\zeta) &= \frac{\tau_\infty K_+(0)}{\zeta K_+(\zeta)} - \frac{F_+(\zeta)}{K_+(\zeta)} \\ (1-\eta v_r \zeta)\, U_- &= -\frac{\tau_\infty K_+(0) K_-(\zeta)}{\mu\zeta} - \frac{F_-(\zeta) K_-(\zeta)}{\mu}, \end{aligned} \tag{A18}$$

where the function $K(\zeta) = K_+(\zeta) K_-(\zeta)$ can be decomposed by inspection

$$\begin{aligned} K_+(\zeta) &= \frac{1}{\sqrt{\lambda_1 + \zeta}} \\ K_-(\zeta) &= \frac{\sqrt{1/\eta v_r - \zeta}}{\sqrt{(\lambda_2 - \zeta)(\lambda_3 - \zeta)}}. \end{aligned} \tag{A19}$$

Here, we derive the solutions of $\tau_+(x)$ and $u_-(x)$ based on the assumption of the cohesive zone model (Equation 9). Considering that the solution of $\tau_+(x)$ in elastic media only involves the function $K_+(\zeta)$, one can readily write $\tau_+(x)$ for the viscoelastic model by replacing λ with λ_1 in Equation 10:

$$\tau_+(x) = \tau_\infty \left(\frac{e^{-\lambda_1 x}}{\sqrt{\pi \lambda_1 x}} + erf\sqrt{\lambda_1 x} \right) - \frac{\tau_c}{\pi} \int_{-\Lambda}^{0} \frac{\sqrt{|\xi|}}{\sqrt{x}} \frac{(\xi/\Lambda + 1)}{x + |\xi|} e^{-\lambda_1 (x+|\xi|)} d\xi, \tag{A20}$$

where the exact value of τ_c for canceling the singularity can be derived by $\lim_{x \to 0^+} \tau_+(x)\sqrt{x} = 0$ and the asymptotic version with the assumption of $\lambda\Lambda \ll 1$ is

$$\frac{\tau_\infty}{\tau_c} \simeq \frac{4\sqrt{\lambda_1 \Lambda}}{3\sqrt{\pi}}. \tag{A21}$$

The detailed inversion for $u_-(x)$ is presented in Appendix A4 and the final result can be written as

$$u(\tilde{x}\Lambda) = \begin{cases} \dfrac{2\tau_\infty}{\mu\lambda_1} \cdot \dfrac{\Lambda}{\eta v_r} \displaystyle\int_0^{|\tilde{x}|} e^{\frac{\Lambda}{\eta v_r}(s - |\tilde{x}|)} \left[\sqrt{\lambda_1}\, \Lambda \int_0^s \phi(\tilde{\rho}\Lambda)\, d\tilde{\rho} - \dfrac{\tau_c \lambda_1 \Lambda^{3/2}}{\tau_\infty \sqrt{\pi}} \int_0^s \phi(\tilde{\rho}\Lambda)\, I(\tilde{\rho} - s)\, d\tilde{\rho} \right] ds, & -1 < \tilde{x} < 0 \\ \dfrac{2\tau_\infty}{\mu\lambda_1} \cdot \dfrac{\Lambda}{\eta v_r} \displaystyle\int_0^{|\tilde{x}|} e^{\frac{\Lambda}{\eta v_r}(s - |\tilde{x}|)} \left[\sqrt{\lambda_1}\, \Lambda \int_0^s \phi(\tilde{\rho}\Lambda)\, d\tilde{\rho} - \dfrac{\tau_c \lambda_1 \Lambda^{3/2}}{\tau_\infty \sqrt{\pi}} \int_{s-1}^s \phi(\tilde{\rho}\Lambda)\, I(\tilde{\rho} - s)\, d\tilde{\rho} \right] ds, & \tilde{x} < -1. \end{cases} \tag{A22}$$

The slip-weakening distance d_c can be derived from Equation A22 at $\tilde{x} = -1$

10.1029/2024JB030663

$$d_c = u(-\Lambda) = \frac{2\tau_\infty \Lambda}{\mu\sqrt{\lambda_1}} \int_0^1 \left(1 - e^{-\frac{\Lambda}{\eta v_r}\left(1-\tilde{\rho}\right)} - \frac{\Lambda}{\eta v_r}\int_0^{1-\tilde{\rho}} (t+\tilde{\rho})^{\frac{3}{2}} e^{-\frac{\Lambda}{\eta v_r}t} dt\right) \phi(\tilde{\rho}\Lambda)\, d\tilde{\rho}. \tag{A23}$$

Because λ_1 is modulated by ηv_r rather than α_s, the solution can be physical even for $v_r > v_s$.

This study focuses on the elongated ruptures with the condition $\eta v_r \ll W$. Since $k_w = 1/\gamma W$, $\eta v_r k_w \ll 1$ and $1/\eta v_r \gg k_w$. Therefore, in the function $\phi(x)$ (defined by Equation A14), where $K_-(\zeta)$ is defined by Equation A19, the dominant contribution comes from the integration path embracing the branch cut between $\zeta = \lambda_2$ and $\zeta = \lambda_3$. Analysis of the cubic equation $\eta v_r \zeta^3 - \alpha_s^2 \zeta^2 + k_w^2 = 0$ shows that if $\eta v_r k_w / \alpha_s^3 \le \frac{2}{3\sqrt{3}}$ there are three real roots and that λ_2 and λ_3 merge at the critical condition, $\eta v_r k_w / \alpha_s^3 = \frac{2}{3\sqrt{3}}$. For subshear rupture, it is thus approximated that

$$\lambda_1 \approx \frac{\lambda_2}{2} \approx \frac{\lambda_3}{2} \approx \left(\frac{k_w^2}{4\eta v_r}\right)^{\frac{1}{3}}, \tag{A24}$$

and the resulting decomposition of Equation A19 becomes

$$\begin{aligned} K_+(\zeta) &= \frac{1}{\sqrt{(\lambda_1 + \zeta)}} \\ K_-(\zeta) &= \frac{\sqrt{1/\eta v_r - \zeta}}{\sqrt{(\lambda_2 - \zeta)(\lambda_3 - \zeta)}} \approx \frac{\sqrt{1/\eta v_r - \zeta}}{2\lambda_1 - \zeta}. \end{aligned} \tag{A25}$$

Because $1/\eta v_r \gg \lambda_1$, $\phi(x) \approx e^{-2\lambda_1 x}/\sqrt{\eta v_r} \approx 1/\sqrt{\eta v_r}$. Therefore, Equation A23 becomes

$$\begin{aligned} d_c &\approx \frac{3\tau_\infty\sqrt{\Lambda}}{\mu\sqrt{\pi k_w}} \cdot \frac{\sqrt{\pi}}{7}\left(\frac{\Lambda}{\eta v_r}\right)^{\frac{3}{2}} \sqrt{\frac{k_w}{\lambda_1}} && \text{if} \quad \Lambda \ll \eta v_r \ll W \\ d_c &\approx \frac{3\tau_\infty\sqrt{\Lambda}}{\mu\sqrt{\pi k_w}} \cdot \frac{2\sqrt{\pi}}{5}\left(\sqrt{\frac{\Lambda}{\eta v_r}} - \frac{5}{3}\sqrt{\frac{\eta v_r}{\Lambda}}\right) \sqrt{\frac{k_w}{\lambda_1}} && \text{if} \quad \eta v_r \ll \Lambda \ll W. \end{aligned} \tag{A26}$$

Substituting Equation A21 into Equation A26 yields the rupture tip equation of motion for subshear ruptures:

$$\begin{aligned} \frac{G_c}{G_0} &\simeq \frac{\sqrt{\pi}}{7}\left(\frac{\Lambda}{\eta v_r}\right)^{\frac{3}{2}} (4\eta v_r k_w)^{\frac{1}{3}} && \text{if} \quad \Lambda \ll \eta v_r \ll W \\ \frac{G_c}{G_0} &\simeq \frac{2\sqrt{\pi}}{5}\left(\sqrt{\frac{\Lambda}{\eta v_r}} - \frac{5}{3}\sqrt{\frac{\eta v_r}{\Lambda}}\right)(4\eta v_r k_w)^{\frac{1}{3}} && \text{if} \quad \eta v_r \ll \Lambda \ll W. \end{aligned} \tag{A27}$$

For supershear cases with $v_r > v_s$ and $\hat{\alpha}_s = \sqrt{(v_r/v_s)^2 - 1} \to 0$, to first order in $\hat{\alpha}_s$, the three roots of the cubic equation $\eta v_r \zeta^3 + \hat{\alpha}_s^2 \zeta^2 + k_w^2 = 0$ can be approximated as

$$\begin{aligned} \lambda_1 &\simeq \left(\frac{k_w^2}{\eta v_r}\right)^{\frac{1}{3}} + \frac{\hat{\alpha}_s^2}{\eta v_r} \\ \lambda_2 &\simeq \frac{1}{2}\left(\frac{k_w^2}{\eta v_r}\right)^{\frac{1}{3}} (1 + \sqrt{3}\, i) \\ \lambda_3 &\simeq \frac{1}{2}\left(\frac{k_w^2}{\eta v_r}\right)^{\frac{1}{3}} (1 - \sqrt{3}\, i), \end{aligned} \tag{A28}$$

where λ_1 and the real parts of λ_2 and λ_3 have the same order of magnitude. Because $\eta v_r k_w \ll 1$, $1/\eta v_r \gg \mathrm{Re}\{\lambda_2\}$ and $\phi(x) \approx e^{-\mathrm{Re}\{\lambda_2\}x}/\sqrt{\eta v_r} \approx 1/\sqrt{\eta v_r}$. Therefore, the rupture tip equation of motion for supershear ruptures is

$$\begin{aligned}\frac{G_c}{G_0} &\simeq \frac{\sqrt{\pi}}{7}\left(\frac{\Lambda}{\eta v_r}\right)^{\frac{3}{2}}\frac{\eta v_r k_w}{(\eta v_r k_w)^{\frac{2}{3}}+\hat{\alpha}_s^2} \qquad \text{if} \quad \Lambda \ll \eta v_r \ll W \\ \frac{G_c}{G_0} &\simeq \frac{2\sqrt{\pi}}{5}\left(\sqrt{\frac{\Lambda}{\eta v_r}}-\frac{5}{3}\sqrt{\frac{\eta v_r}{\Lambda}}\right)\frac{\eta v_r k_w}{(\eta v_r k_w)^{\frac{2}{3}}+\hat{\alpha}_s^2} \qquad \text{if} \quad \eta v_r \ll \Lambda \ll W.\end{aligned} \tag{A29}$$

For fast supershear ruptures with $\hat{\alpha}_s \gg (\eta v_r k_w)^{\frac{1}{3}}$, the above solution asymptotically becomes

$$\begin{aligned}G_c &\simeq \frac{\sqrt{\pi}}{7}\left(\frac{\Lambda}{\eta v_r}\right)^{\frac{3}{2}}\frac{\Delta\tau^2\eta v_r}{\hat{\alpha}_s^2\mu} \propto \frac{\Delta\tau^2\Lambda^{\frac{3}{2}}}{\hat{\alpha}_s^2\mu\sqrt{\eta v_r}} \qquad \text{if} \quad \Lambda \ll \eta v_r \ll W \\ G_c &\simeq \frac{2\sqrt{\pi}}{5}\left(\sqrt{\frac{\Lambda}{\eta v_r}}-\frac{5}{3}\sqrt{\frac{\eta v_r}{\Lambda}}\right)\frac{\Delta\tau^2\eta v_r}{\hat{\alpha}_s^2\mu} \propto \frac{\Delta\tau^2\sqrt{\eta v_r\Lambda}}{\hat{\alpha}_s^2\mu} \qquad \text{if} \quad \eta v_r \ll \Lambda \ll W.\end{aligned} \tag{A30}$$

For small rupture speed $\alpha_s \simeq 1$, the three real roots of the cubic equation $\eta v_r\zeta^3 - \alpha_s^2\zeta^2 + k_w^2 = 0$ can be approximated as $\lambda_1 \simeq \lambda_2 \simeq k_w$ and $\lambda_3 \simeq 1/\eta v_r$. Thus $K_-(\zeta) \approx 1/\sqrt{\lambda_2 - \zeta}$ and $\phi(x) \approx e^{-k_w x}/\sqrt{\pi x}$. The critical slip-weakening distance d_c can be derived as

$$d_c \approx \frac{3\tau_\infty\sqrt{\Lambda}}{\mu\sqrt{\pi k_w}}\left(1-\frac{\eta v_r}{\Lambda}\right), \qquad \text{if} \quad \eta v_r \ll \Lambda \ll W. \tag{A31}$$

Therefore, the equivalent fracture energy for slow ruptures can be written as

$$G_0 = G_{\text{equiv}} \approx G_c\left(1+2\frac{\eta v_r}{\Lambda}\right), \tag{A32}$$

where a correction of a factor of 2 is made to fit the numerical results.

A3. Attenuation and Velocity Dispersion of Plane Waves in Viscoelasticity

Assuming a plane wave propagating along the x axis in a viscoelastic medium, the 2.5D governing equation can be written as

$$\left(1+\eta\frac{\partial}{\partial t}\right)\frac{\partial^2 u(x,t)}{\partial x^2} - k_w^2 u(x,t) = \frac{1}{v_s^2}\frac{\partial^2 u(x,t)}{\partial t^2}. \tag{A33}$$

Applying the Fourier transform to the above equation yields

$$\frac{\partial^2 U}{\partial x^2} = -\frac{\omega^2/v_s^2 - k_w^2}{1+i\omega\eta}U, \tag{A34}$$

where

$$U(\omega) = \int_{-\infty}^{\infty} u(x,t)e^{-i\omega t}dt. \tag{A35}$$

The general solution can be given in the form of

$$U(\omega) = U_0 e^{-A(\omega)x - iB(\omega)x}, \tag{A36}$$

where $A(\omega)$ and $B(\omega)$ are two undetermined functions. Substituting Equation A36 into Equation A34 yields

$$(A + iB)^2 = \frac{\omega_w^2}{v_s^2} \cdot \frac{(\omega/\omega_w)^2 - 1}{(\omega/\omega_v)^2 + 1}(i\omega/\omega_v - 1), \tag{A37}$$

where $\omega_w \equiv k_w v_s$ and $\omega_v \equiv 1/\eta$. Since $k_w \eta v_s \ll 1$, $\omega_w \ll \omega_v$ in this study. The complex function on the right side can be written as

$$i\omega/\omega_v - 1 = (a + ib)^2, \quad a = \frac{1}{\sqrt{2}}\sqrt{\sqrt{1 + (\omega/\omega_v)^2} - 1}, \quad b = \frac{1}{\sqrt{2}}\sqrt{\sqrt{1 + (\omega/\omega_v)^2} + 1}. \tag{A38}$$

Thus, the solution for $\omega > \omega_w$ is

$$\begin{aligned} A(\omega) &= \frac{\omega_w\sqrt{(\omega/\omega_w)^2 - 1}}{\sqrt{2}v_s} \cdot \sqrt{\frac{1}{\sqrt{1 + (\omega/\omega_v)^2}} - \frac{1}{1 + (\omega/\omega_v)^2}} \\ B(\omega) &= \frac{\omega_w\sqrt{(\omega/\omega_w)^2 - 1}}{\sqrt{2}v_s} \cdot \sqrt{\frac{1}{\sqrt{1 + (\omega/\omega_v)^2}} + \frac{1}{1 + (\omega/\omega_v)^2}}. \end{aligned} \tag{A39}$$

Specifically for $\omega_w = 0$, the model becomes 2D and the solution is

$$\begin{aligned} A(\omega) &= \frac{\omega}{\sqrt{2}v_s} \cdot \sqrt{\frac{1}{\sqrt{1 + (\omega/\omega_v)^2}} - \frac{1}{1 + (\omega/\omega_v)^2}} \\ B(\omega) &= \frac{\omega}{\sqrt{2}v_s} \cdot \sqrt{\frac{1}{\sqrt{1 + (\omega/\omega_v)^2}} + \frac{1}{1 + (\omega/\omega_v)^2}}. \end{aligned} \tag{A40}$$

$\tilde{A} = A(\omega)/(\omega_w/v_s)$ and $\tilde{V} = \omega/B(\omega)v_s$ are defined as the normalized attenuation of plane waves and the normalized phase velocity dispersion, respectively. The 2.5D and 2D solutions of plane waves are remarkably similar at high frequency. It is noted that the approximated term of finite fault width in the 2.5D model causes "standing waves" at $\omega/\omega_w < 1$, which may explain why the 3D rupture tip equation of motion in elastic media has "inertia" while the 2D one does not (Weng & Ampuero, 2019). The velocity dispersion at high frequency in viscoelasticity is supposed to be the primary reason for explaining the unbounded speeds of frictional ruptures.

A4. Inversions of Laplace Transforms

A4.1. Elastic Rupture Problem

The formal inversions of T_+ and U_- are

$$\begin{aligned} \tau_+(x) &= \frac{1}{2\pi i}\int_{\epsilon - i\infty}^{\epsilon + i\infty}\left[\frac{\tau_\infty K_+(0)}{\zeta K_+(\zeta)} - \frac{F_+(\zeta)}{K_+(\zeta)}\right]e^{\zeta x}d\zeta \qquad \text{for} \quad x > 0 \\ u_-(x) &= \frac{1}{2\pi i}\int_{\epsilon - i\infty}^{\epsilon + i\infty}\left[-\frac{\tau_\infty K_+(0)K_-(\zeta)}{\mu\zeta} - \frac{F_-(\zeta)K_-(\zeta)}{\mu}\right]e^{\zeta x}d\zeta \qquad \text{for} \quad x < 0, \end{aligned} \tag{A41}$$

where ϵ is a real number in the interval $-\lambda < \epsilon < 0$. The first term on the right side of Equation A41 for $\tau_+(x)$ can be solved by differentiating with respect to x, then integrating over ζ, and finally by integrating again with respect to x, so

$$\frac{1}{2\pi i}\int_{\epsilon-i\infty}^{\epsilon+i\infty}\frac{\tau_\infty K_+(0)}{\zeta K_+(\zeta)}e^{\zeta x}d\zeta=\tau_\infty+\frac{\tau_\infty}{2\sqrt{\pi\lambda}}\int_x^\infty\frac{e^{-\lambda\xi}}{\xi^{3/2}}d\xi. \tag{A42}$$

The function $F_+(\zeta)$ can be evaluated by shifting the integral contour C_+ to the paths that embrace the left branch cut $\zeta' < -\lambda$ and changing the sign of the integral variable

$$\begin{aligned}F_+(\zeta)&=-\frac{1}{2\pi i}\int_{C_+}\frac{K_+(\zeta')T_-(\zeta')}{\zeta'-\zeta}d\zeta'\\&=-\frac{1}{\pi}\int_{-\infty}^0\tau_f(\xi)d\xi\int_{-\lambda}^{-\infty}\mathrm{Im}\,\frac{e^{-\zeta'\xi}}{(\zeta'-\zeta)\sqrt{\alpha_s(\zeta'+\lambda)}}d\zeta'\\&=\frac{1}{\pi}\int_{-\infty}^0\tau_f(\xi)d\xi\int_\lambda^\infty\frac{e^{\zeta'\xi}}{(\zeta'+\zeta)\sqrt{\alpha_s(\zeta'-\lambda)}}d\zeta',\end{aligned} \tag{A43}$$

where Im {} is a function that returns the imaginary part of a complex number. So the second term on the right side of Equation A41 for $\tau_+(x)$ can be solved by shifting the integral contour onto the left branch cut $\zeta' < -\lambda$

$$\begin{aligned}&-\frac{1}{2\pi i}\int_{\epsilon-i\infty}^{\epsilon+i\infty}\frac{F_+(\zeta)}{K_+(\zeta)}e^{\zeta x}d\zeta\\&=-\frac{1}{2\pi^2 i}\int_{-\infty}^0\tau_f(\xi)d\xi\int_\lambda^\infty d\zeta'\int_{\epsilon-i\infty}^{\epsilon+i\infty}\frac{e^{\zeta'\xi+\zeta x}}{K_+(\zeta)(\zeta'+\zeta)\sqrt{\alpha_s(\zeta'-\lambda)}}d\zeta\\&=-\frac{1}{\pi^2}\int_{-\infty}^0\tau_f(\xi)d\xi\int_\lambda^\infty d\zeta'\int_{-\lambda}^{-\infty}\mathrm{Im}\left\{\frac{e^{\zeta'\xi+\zeta x}}{K_+(\zeta)(\zeta'+\zeta)\sqrt{\alpha_s(\zeta'-\lambda)}}\right\}d\zeta\\&=-\frac{1}{\pi^2}\int_{-\infty}^0\tau_f(\xi)d\xi\int_\lambda^\infty d\zeta'\int_\lambda^\infty\frac{\sqrt{\zeta-\lambda}}{(\zeta-\zeta')\sqrt{\zeta'-\lambda}}e^{-\zeta'|\xi|-\zeta x}d\zeta\\&=-\frac{1}{\pi^2}\int_{-\infty}^0 e^{-\lambda(x+|\xi|)}\tau_f(\xi)d\xi\int_0^\infty\int_0^\infty\frac{\sqrt{\zeta}}{(\zeta-\zeta')\sqrt{\zeta'}}e^{-\zeta'|\xi|-\zeta x}d\zeta d\zeta'\\&=-\frac{1}{\pi}\int_{-\infty}^0\frac{\sqrt{|\xi|}}{\sqrt{x}}\frac{1}{x+|\xi|}e^{-\lambda(x+|\xi|)}\tau_f(\xi)d\xi,\end{aligned} \tag{A44}$$

where the double integrals can be evaluated with the assistance of either Mathematica or the Tables of Integral Transforms (Erdélyi et al., 1954).

Therefore,

$$\tau_+(x)=\tau_\infty+\frac{\tau_\infty}{2\sqrt{\pi\lambda}}\int_x^\infty\frac{e^{-\lambda\xi}}{\xi^{3/2}}d\xi-\frac{1}{\pi}\int_{-\infty}^0\frac{\sqrt{|\xi|}}{\sqrt{x}}\frac{1}{x+|\xi|}e^{-\lambda(x+|\xi|)}\tau_f(\xi)d\xi. \tag{A45}$$

The first term on the right side of Equation A41 for $u_-(x)$ can be solved by differentiating with respect to $|x|$, then integrating over ζ, and finally by integrating again with respect to $|x|$

$$\begin{aligned}-\frac{1}{2\pi i}\int_{\delta-i\infty}^{\delta+i\infty}\frac{\tau_\infty K_+(0)K_-(\zeta)}{\mu\zeta}e^{\zeta x}d\zeta&=-\frac{1}{2\pi i}\int_{\delta-i\infty}^{\delta+i\infty}\frac{\tau_\infty K_+(0)K_-(\zeta)}{\mu\zeta}e^{-\zeta|x|}d\zeta\\&=\frac{\tau_\infty}{\mu\sqrt{k_w}}\int_0^{|x|}\phi(\rho)d\rho,\end{aligned} \tag{A46}$$

where

10.1029/2024JB030663

$$\phi(\rho) = \frac{1}{2\pi i}\int_{\delta-i\infty}^{\delta+i\infty} K_{-}(\zeta)e^{-\zeta\rho}d\zeta = \frac{e^{-\lambda\rho}}{\sqrt{\pi\alpha_s\rho}} \qquad \text{for} \quad \rho > 0. \tag{A47}$$

Note that $\phi(\rho) = 0$ for $\rho < 0$ because all singularities in $K_{-}(\zeta)$ lie in the right half plane $\mathrm{Re}\{\zeta\} > 0$.

According to the decomposition of Cauchy's theorem, the function $F_{-}(\zeta)$ can be readily written

$$\begin{aligned} F_{-}(\zeta) &= -F_{+}(\zeta) + K_{+}(\zeta)T_{-}(\zeta) \\ &= -\frac{1}{\pi}\int_{-\infty}^{0}\tau_f(\xi)d\xi\int_{\lambda}^{\infty}\frac{e^{\zeta'\xi}}{(\zeta'+\zeta)\sqrt{\alpha_s(\zeta'-\lambda)}}d\zeta' + \int_{-\infty}^{0}\tau_f(\xi)K_{+}(\zeta)e^{-\zeta\xi}d\xi. \end{aligned} \tag{A48}$$

So the second term on the right side of Equation A41 for $u_{-}(x)$ can be solved

$$\begin{aligned} &-\frac{1}{2\pi i}\int_{\delta-i\infty}^{\delta+i\infty}\frac{F_{-}(\zeta)K_{-}(\zeta)}{\mu}e^{\zeta x}d\zeta = \\ &\frac{1}{2\pi^2 i\mu}\int_{\delta-i\infty}^{\delta+i\infty}\int_{-\infty}^{0}\tau_f(\xi)d\xi\int_{\lambda}^{\infty}\frac{e^{\zeta'\xi}}{(\zeta'+\zeta)\sqrt{\alpha_s(\zeta'-\lambda)}}d\zeta'\cdot K_{-}(\zeta)e^{\zeta x}d\zeta \\ &-\frac{1}{2\pi i\mu}\int_{\delta-i\infty}^{\delta+i\infty}\int_{-\infty}^{0}\tau_f(\xi)K_{+}(\zeta)K_{-}(\zeta)e^{\zeta(x-\xi)}d\zeta d\xi \\ &= \frac{1}{2\pi i\mu}\int_{\delta-i\infty}^{\delta+i\infty}\int_{-\infty}^{0}\tau_f(\xi)erfc\sqrt{|\xi|(\zeta+\lambda)}K_{+}(\zeta)\cdot K_{-}(\zeta)e^{\zeta(x-\xi)}d\zeta d\xi \\ &-\frac{1}{2\pi i\mu}\int_{\delta-i\infty}^{\delta+i\infty}\int_{-\infty}^{0}\tau_f(\xi)K_{+}(\zeta)K_{-}(\zeta)e^{\zeta(x-\xi)}d\zeta d\xi \\ &= -\frac{1}{2\pi i\mu}\int_{\delta-i\infty}^{\delta+i\infty}\int_{-\infty}^{0}\tau_f(\xi)erf\sqrt{|\xi|(\zeta+\lambda)}K_{+}(\zeta)\cdot K_{-}(\zeta)e^{\zeta(x-\xi)}d\zeta d\xi \\ &= -\frac{1}{2\pi i\mu}\int_{\delta-i\infty}^{\delta+i\infty}\int_{-\infty}^{0}\tau_f(\xi)d\xi\left[\frac{\sqrt{|\xi|(\zeta+\lambda)}}{\sqrt{\pi}}\int_0^1\frac{e^{-|\xi|(\zeta+\lambda)t}}{\sqrt{t}}dt\right]K_{+}(\zeta)\cdot K_{-}(\zeta)e^{\zeta(x-\xi)}d\zeta \\ &= -\frac{1}{2\pi i\mu\sqrt{\alpha_s}}\int_{\delta-i\infty}^{\delta+i\infty}\int_{-\infty}^{0}\tau_f(\xi)d\xi\left[\int_0^1\frac{\sqrt{|\xi|}}{\sqrt{\pi}}\frac{e^{-\zeta(\xi-x-\xi t)+\xi\lambda t}}{\sqrt{t}}dt\right]\cdot K_{-}(\zeta)d\zeta, \end{aligned} \tag{A49}$$

where an integral representation for the function $erf()$ is used (Ng & Geller, 1969) and $K_{+}(\zeta)\sqrt{\zeta+\lambda} = 1/\sqrt{\alpha_s}$. After changing the integral variables to $\rho = \xi - x - \xi t$ and exchanging the order of integration in the above equation, and substituting into Equation A41, the complete solution for $u_{-}(x)$ is:

$$u_{-}(x) = \frac{\tau_\infty}{\mu\sqrt{k_w}}\int_0^{-x}\phi(\rho)d\rho - \frac{1}{\mu\sqrt{\pi\alpha_s}}\int_{-\infty}^{0}\tau_f(\xi)d\xi\int_{\max(0,\xi-x)}^{-x}\frac{e^{-\lambda(\rho-\xi+x)}}{\sqrt{\rho-\xi+x}}\phi(\rho)d\rho, \tag{A50}$$

where the function $\max(0, \xi - x)$ is used because $\phi(\rho) = 0$ when $\rho < 0$. Changing the integral order for the second term, the above equation can be written as

$$u_{-}(x) = \frac{\tau_\infty}{\mu\sqrt{k_w}}\int_0^{-x}\phi(\rho)d\rho - \frac{1}{\mu\sqrt{\pi\alpha_s}}\int_0^{-x}\phi(\rho)d\rho\int_{-\infty}^{\rho+x}\frac{e^{-\lambda(\rho-\xi+x)}}{\sqrt{\rho-\xi+x}}\tau_f(\xi)d\xi. \tag{A51}$$

A4.2. Viscoelastic Rupture Problem

To invert $u_{-}(x)$ for the viscoelastic model, it is needed to first invert $(1 - \eta v_r\zeta)\,U_{-}(\zeta)$. The inversion of $(1 - \eta v_r\zeta)\,U_{-}(\zeta)$ can be done by a similar way for inverting $u_{-}(x)$ in the elastic model

$$\begin{aligned} w(x) &= L^{-1}((1-\eta v_r\zeta)\,U_-)(x) \\ &= \frac{1}{2\pi i}\int_{\epsilon-i\infty}^{\epsilon+i\infty}\left[-\frac{\tau_\infty K_+(0)K_-(\zeta)}{\mu\zeta}-\frac{F_-(\zeta)K_-(\zeta)}{\mu}\right]e^{\zeta x}d\zeta. \end{aligned} \tag{A52}$$

The first term on the right side is

$$\begin{aligned} -\frac{1}{2\pi i}\int_{\delta-i\infty}^{\delta+i\infty}\frac{\tau_\infty K_+(0)K_-(\zeta)}{\mu\zeta}e^{\zeta x}d\zeta &= -\frac{1}{2\pi i}\int_{\delta-i\infty}^{\delta+i\infty}\frac{\tau_\infty K_+(0)K_-(\zeta)}{\mu\zeta}e^{-\zeta|x|}d\zeta \\ &= \frac{\tau_\infty}{\mu\sqrt{\lambda_1}}\int_0^{|x|}\phi(\rho)d\rho, \end{aligned} \tag{A53}$$

where

$$\phi(\rho) = \frac{1}{2\pi i}\int_{\delta-i\infty}^{\delta+i\infty}K_-(\zeta)e^{-\zeta\rho}d\zeta \qquad \text{for} \quad \rho > 0, \tag{A54}$$

which includes all singularities in the right half plane $\mathrm{Re}\{\zeta\} > 0$. The second term on the right side is

$$\begin{aligned} &-\frac{1}{2\pi i}\int_{\delta-i\infty}^{\delta+i\infty}\frac{F_-(\zeta)K_-(\zeta)}{\mu}e^{\zeta x}d\zeta \\ &= -\frac{1}{2\pi i\mu}\int_{\delta-i\infty}^{\delta+i\infty}\int_{-\infty}^{0}\tau_f(\xi)d\xi\left[\int_0^1\frac{\sqrt{|\xi|}}{\sqrt{\pi}}\,\frac{e^{-\zeta(\xi-x-\xi t)+\xi\lambda_1 t}}{\sqrt{t}}dt\right]\cdot K_-(\zeta)d\zeta, \end{aligned} \tag{A55}$$

where $K_+(\zeta)\sqrt{\zeta+\lambda_1} = 1$ is used. Therefore,

$$w(x) = \frac{\tau_\infty}{\mu\sqrt{\lambda_1}}\int_0^{-x}\phi(\rho)d\rho - \frac{1}{\mu\sqrt{\pi}}\int_{-\infty}^{0}\tau_f(\xi)d\xi\int_{\max(0,\xi-x)}^{-x}\frac{e^{-\lambda_1(\rho-\xi+x)}}{\sqrt{\rho-\xi+x}}\phi(\rho)d\rho. \tag{A56}$$

Finally, the inversion of $u_-(x)$ can be derived by

$$u_-(x) = \frac{1}{\eta v_r}\int_0^{|x|}e^{\frac{l-|x|}{\eta v_r}}w(-l)dl. \tag{A57}$$

Substituting $\tau_f(\xi)$ and normalizing all the distances by $s = l/\Lambda$, $\tilde{\xi} = \xi/\Lambda$, $\tilde{x} = x/\Lambda$, and $\tilde{\rho} = \rho/\Lambda$ yield

$$u(\tilde{x}\Lambda) = \begin{cases} \dfrac{2\tau_\infty}{\mu\lambda_1}\cdot\dfrac{\Lambda}{\eta v_r}\displaystyle\int_0^{|\tilde{x}|}e^{\frac{\Lambda}{\eta v_r}\left(s-|\tilde{x}|\right)}\left[\sqrt{\lambda_1}\,\Lambda\int_0^s\phi(\tilde{\rho}\Lambda)\,d\tilde{\rho}-\dfrac{\tau_c\lambda_1\Lambda^{3/2}}{\tau_\infty\sqrt{\pi}}\int_0^s\phi(\tilde{\rho}\Lambda)\,I(\tilde{\rho}-s)\,d\tilde{\rho}\right]ds, & -1<\tilde{x}<0 \\ \dfrac{2\tau_\infty}{\mu\lambda_1}\cdot\dfrac{\Lambda}{\eta v_r}\displaystyle\int_0^{|\tilde{x}|}e^{\frac{\Lambda}{\eta v_r}\left(s-|\tilde{x}|\right)}\left[\sqrt{\lambda_1}\,\Lambda\int_0^s\phi(\tilde{\rho}\Lambda)\,d\tilde{\rho}-\dfrac{\tau_c\lambda_1\Lambda^{3/2}}{\tau_\infty\sqrt{\pi}}\int_{s-1}^s\phi(\tilde{\rho}\Lambda)\,I(\tilde{\rho}-s)\,d\tilde{\rho}\right]ds, & \tilde{x}<-1, \end{cases} \tag{A58}$$

where the inner function $I()$ is defined as

$$I(s) \equiv \int_{-1}^{s}\frac{(1+t)e^{-\lambda\Lambda(s-t)}}{\sqrt{s-t}}dt \simeq \frac{4}{3}(1+s)^{3/2}, \qquad \text{for} \quad s<0. \tag{A59}$$

This paper focuses on the condition of $-1 < \tilde{x} < 0$ for the energy balance. Substituting the relation between τ_c and τ_∞ (Equation A21) into Equation A58 yields

$$u(\tilde{x}\Lambda) = \frac{2\tau_\infty \Lambda}{\mu\sqrt{\lambda_1}} \cdot \int_0^{|\tilde{x}|} \frac{\Lambda}{\eta v_r} e^{\frac{\Lambda}{\eta v_r}\left(s-|\tilde{x}|\right)} ds \int_0^s \phi(\tilde{\rho}\Lambda)\left[1-(1+\tilde{\rho}-s)^{\frac{3}{2}}\right] d\tilde{\rho}. \tag{A60}$$

Therefore, the slip-weakening distance d_c is

$$\begin{aligned} d_c = u(-\Lambda) &= \frac{2\tau_\infty \Lambda}{\mu\sqrt{\lambda_1}} \int_0^1 \frac{\Lambda}{\eta v_r} e^{-\frac{\Lambda}{\eta v_r}(1-s)} ds \int_0^s \phi(\tilde{\rho}\Lambda)\left[1-(1+\tilde{\rho}-s)^{\frac{3}{2}}\right] d\tilde{\rho} \\ &= \frac{2\tau_\infty \Lambda}{\mu\sqrt{\lambda_1}} \int_0^1 \phi(\tilde{\rho}\Lambda)\, d\tilde{\rho} \int_{\tilde{\rho}}^1 \frac{\Lambda}{\eta v_r}\left[1-(1+\tilde{\rho}-s)^{\frac{3}{2}}\right] e^{-\frac{\Lambda}{\eta v_r}(1-s)} ds \\ &= \frac{2\tau_\infty \Lambda}{\mu\sqrt{\lambda_1}} \int_0^1 \left(1 - e^{-\frac{\Lambda}{\eta v_r}\left(1-\tilde{\rho}\right)} - \frac{\Lambda}{\eta v_r} \int_0^{1-\tilde{\rho}} (t+\tilde{\rho})^{\frac{3}{2}} e^{-\frac{\Lambda}{\eta v_r} t} dt\right) \phi(\tilde{\rho}\Lambda)\, d\tilde{\rho}. \end{aligned} \tag{A61}$$

Data Availability Statement

No data sets were generated or analyzed during the current study. The theoretical derivations are presented in the manuscript. The open source software SEM2DPACK for the 2.5D and 2D simulations is available from https://github.com/jpampuero/sem2dpack and the open source software SPECFEM3D for the 3D simulations is available from the Computational Infrastructure for Geodynamics at https://geodynamics.org/resources/specfem3dcartesian. An example of a finite thickness fault zone with Kelvin–Voigt viscoelasticity is available in the "Kelvin_Visco_FZ" folder of the GitHub repository at https://github.com/jpampuero/sem2dpack/tree/master/EXAMPLES/.

Acknowledgments
This work was supported by the National Natural Science Foundation of China (42374066) and the National Key Research and Development Program of China (2023YFC3007302). The author thanks Robert Viesca for his suggestions in clarifying the research context for viscoelastic ruptures in the manuscript. The author also benefited from discussions with Eric Dunham, Yoshihiro Kaneko, Chao Liang, and Alice-Agnes Gabriel and is thankful to the Editor, Associate Editor, and the anonymous reviewers for their constructive feedback and thoughtful suggestions, which significantly improved the manuscript.

References

Ampuero, J.-P. (2012). *Sem2dpack, a spectral element software for 2d seismic wave propagation and earthquake source dynamics, v2.3.8*. Zenodo. https://doi.org/10.5281/zenodo.230363

Ando, R., Takeda, N., & Yamashita, T. (2012). Propagation dynamics of seismic and aseismic slip governed by fault heterogeneity and Newtonian rheology. *Journal of Geophysical Research*, *117*(B11), B11308. https://doi.org/10.1029/2012jb009532

Andrews, D. J. (1976). Rupture propagation with finite stress in antiplane strain. *Journal of Geophysical Research*, *81*(20), 3575–3582. https://doi.org/10.1029/jb081i020p03575

Andrews, D. J. (2005). Rupture dynamics with energy loss outside the slip zone. *Journal of Geophysical Research*, *110*(B1), B01307. https://doi.org/10.1029/2004jb003191

Åström, J., Herrmann, H., & Timonen, J. (2000). Granular packings and fault zones. *Physical Review Letters*, *84*(4), 638.

Barber, M., Donley, J., & Langer, J. S. (1989). Steady-state propagation of a crack in a viscoelastic strip. *Physical Review A*, *40*(1), 366–376. https://doi.org/10.1103/physreva.40.366

Barbot, S. (2019). Slow-slip, slow earthquakes, period-two cycles, full and partial ruptures, and deterministic chaos in a single asperity fault. *Tectonophysics*, *768*, 228171. https://doi.org/10.1016/j.tecto.2019.228171

Beall, A., Fagereng, A., & Ellis, S. (2019). Strength of strained two-phase mixtures: Application to rapid creep and stress amplification in subduction zone mélange. *Geophysical Research Letters*, *46*(1), 169–178. https://doi.org/10.1029/2018gl081252

Behr, W. M., & Bürgmann, R. (2021). What's down there? The structures, materials and environment of deep-seated slow slip and tremor. *Philosophical Transactions of the Royal Society A: Mathematical, Physical and Engineering Sciences*, *379*(2193), 20200218. https://doi.org/10.1098/rsta.2020.0218

Behr, W. M., Gerya, T. V., Cannizzaro, C., & Blass, R. (2021). Transient slow slip characteristics of frictional-viscous subduction megathrust shear zones. *AGU Advances*, *2*(3), e2021AV000416. https://doi.org/10.1029/2021av000416

Behr, W. M., Kotowski, A. J., & Ashley, K. T. (2018). Dehydration-induced rheological heterogeneity and the deep tremor source in warm subduction zones. *Geology*, *46*(5), 475–478. https://doi.org/10.1130/g40105.1

Ben-Zion, Y. (1998). Properties of seismic fault zone waves and their utility for imaging low-velocity structures. *Journal of Geophysical Research*, *103*(B6), 12567–12585. https://doi.org/10.1029/98jb00768

Ben-Zion, Y., & Lyakhovsky, V. (2019). Representation of seismic sources sustaining changes of elastic moduli. *Geophysical Journal International*, *217*(1), 135–139. https://doi.org/10.1093/gji/ggz018

Beroza, G. C., & Ide, S. (2011). Slow earthquakes and nonvolcanic tremor. *Annual Review of Earth and Planetary Sciences*, *39*(1), 271–296. https://doi.org/10.1146/annurev-earth-040809-152531

Bhattacharya, P., & Viesca, R. C. (2019). Fluid-induced aseismic fault slip outpaces pore-fluid migration. *Science*, *364*(6439), 464–468. https://doi.org/10.1126/science.aaw7354

Buehler, M. J., Abraham, F. F., & Gao, H. (2003). Hyperelasticity governs dynamic fracture at a critical length scale. *Nature*, *426*(6963), 141–146. https://doi.org/10.1038/nature02096

Burridge, R. (1973). Admissible speeds for plane-strain self-similar shear cracks with friction but lacking cohesion. *Geophysical Journal International*, *35*(4), 439–455. https://doi.org/10.1111/j.1365-246X.1973.tb00608.x

Carbone, G., & Persson, B. N. (2005). Hot cracks in rubber: Origin of the giant toughness of rubberlike materials. *Physical Review Letters*, *95*(11), 114301. https://doi.org/10.1103/PhysRevLett.95.114301

Cattania, C., & Segall, P. (2021). Precursory slow slip and foreshocks on rough faults. *Journal of Geophysical Research: Solid Earth*, *126*(4), e2020JB020430. https://doi.org/10.1029/2020jb020430
Chen, C.-H., Bouchbinder, E., & Karma, A. (2017). Instability in dynamic fracture and the failure of the classical theory of cracks. *Nature Physics*, *13*(12), 1186–1190. https://doi.org/10.1038/nphys4237
Chounet, A., Vallée, M., Causse, M., & Courboulex, F. (2018). Global catalog of earthquake rupture velocities shows anticorrelation between stress drop and rupture velocity. *Tectonophysics*, *733*, 148–158. https://doi.org/10.1016/j.tecto.2017.11.005
Dal Zilio, L., Lapusta, N., & Avouac, J. (2020). Unraveling scaling properties of slow-slip events. *Geophysical Research Letters*, *47*(10), e2020GL087477. https://doi.org/10.1029/2020gl087477
Dieterich, J. H. (1979). Modeling of rock friction: 1. Experimental results and constitutive equations. *Journal of Geophysical Research*, *84*(B5), 2161–2168. https://doi.org/10.1029/jb084ib05p02161
Dong, P., Xia, K., Xu, Y., Elsworth, D., & Ampuero, J. P. (2023). Laboratory earthquakes decipher control and stability of rupture speeds. *Nature Communications*, *14*(1), 2427. https://doi.org/10.1038/s41467-023-38137-w
Dragert, H., Wang, K., & James, T. S. (2001). A silent slip event on the deeper cascadia subduction interface. *Science*, *292*(5521), 1525–1528. https://doi.org/10.1126/science.1060152
Dunham, E. M. (2007). Conditions governing the occurrence of supershear ruptures under slip-weakening friction. *Journal of Geophysical Research*, *112*(B7), B07302. https://doi.org/10.1029/2006JB004717
Dunham, E. M., & Bhat, H. S. (2008). Attenuation of radiated ground motion and stresses from three-dimensional supershear ruptures. *Journal of Geophysical Research*, *113*(B8), B08319. https://doi.org/10.1029/2007jb005182
Erdélyi, A., Magnus, W., Oberhettinger, F., & Tricomi, F. G. (1954). *Tables of integral transforms*. McGRAW-HILL BOOK COMPANY, INC.
Fagereng, A., & Beall, A. (2021). Is complex fault zone behaviour a reflection of rheological heterogeneity? *Philosophical transactions. Series A, Mathematical, physical, and engineering sciences*, *379*(2193), 20190421. https://doi.org/10.1098/rsta.2019.0421
Fagereng, A., & den Hartog, S. A. M. (2016). Subduction megathrust creep governed by pressure solution and frictional-viscous flow. *Nature Geoscience*, *10*(1), 51–57. https://doi.org/10.1038/ngeo2857
Fan, L. F., Ren, F., & Ma, G. W. (2011). Experimental study on viscoelastic behavior of sedimentary rock under dynamic loading. *Rock Mechanics and Rock Engineering*, *45*(3), 433–438. https://doi.org/10.1007/s00603-011-0197-7
Freund, L. (1998). *Dynamic fracture mechanics*. Cambridge University Press.
Galvez, P., Ampuero, J.-P., Dalguer, L. A., Somala, S. N., & Nissen-Meyer, T. (2014). Dynamic earthquake rupture modelled with an unstructured 3-D spectral element method applied to the 2011 *M*9 Tohoku earthquake. *Geophysical Journal International*, *198*(2), 1222–1240. https://doi.org/10.1093/gji/ggu203
Gao, K., Euser, B. J., Rougier, E., Guyer, R. A., Lei, Z., Knight, E. E., et al. (2018). Modeling of stick-slip behavior in sheared granular fault gouge using the combined finite-discrete element method. *Journal of Geophysical Research: Solid Earth*, *123*(7), 5774–5792. https://doi.org/10.1029/2018jb015668
Goldman, T., Livne, A., & Fineberg, J. (2010). Acquisition of inertia by a moving crack. *Physical Review Letters*, *104*(11), 114301. https://doi.org/10.1103/physrevlett.104.114301
Gori, M., Rubino, V., Rosakis, A. J., & Lapusta, N. (2018). Pressure shock fronts formed by ultra-fast shear cracks in viscoelastic materials. *Nature Communications*, *9*(1), 4754. https://doi.org/10.1038/s41467-018-07139-4
Greenwood, J., & Johnson, K. (1981). The mechanics of adhesion of viscoelastic solids. *Philosophical Magazine A*, *43*(3), 697–711. https://doi.org/10.1080/01418618108240402
Gumbsch, P., & Gao, H. (1999). Dislocations faster than the speed of sound. *Science*, *283*(5404), 965–968. https://doi.org/10.1126/science.283.5404.965
Guozden, T. M., Jagla, E. A., & Marder, M. (2010). Supersonic cracks in lattice models. *International Journal of Fracture*, *162*(1), 107–125. https://doi.org/10.1007/s10704-009-9426-4
Hawthorne, J., & Rubin, A. (2013). Laterally propagating slow slip events in a rate and state friction model with a velocity-weakening to velocity-strengthening transition. *Journal of Geophysical Research: Solid Earth*, *118*(7), 3785–3808. https://doi.org/10.1002/jgrb.50261
Hirose, H., Hirahara, K., Kimata, F., Fujii, N., & Miyazaki, S. (1999). A slow thrust slip event following the two 1996 Hyuganada earthquakes beneath the Bungo Channel, southwest Japan. *Geophysical Research Letters*, *26*(21), 3237–3240. https://doi.org/10.1029/1999gl010999
Houston, H., Delbridge, B. G., Wech, A. G., & Creager, K. C. (2011). Rapid tremor reversals in Cascadia generated by a weakened plate interface. *Nature Geoscience*, *4*(6), 404–409. https://doi.org/10.1038/ngeo1157
Huang, Y., Ampuero, J., & Helmberger, D. V. (2014). Earthquake ruptures modulated by waves in damaged fault zones. *Journal of Geophysical Research: Solid Earth*, *119*(4), 3133–3154. https://doi.org/10.1002/2013jb010724
Hui, C.-Y., Xu, D.-B., & Kramer, E. J. (1992). A fracture model for a weak interface in a viscoelastic material (small scale yielding analysis). *Journal of Applied Physics*, *72*(8), 3294–3304. https://doi.org/10.1063/1.351451
Ida, Y. (1972). Cohesive force across the tip of a longitudinal-shear crack and griffith's specific surface energy. *Journal of Geophysical Research*, *77*(20), 3796–3805. https://doi.org/10.1029/jb077i020p03796
Ide, S., Beroza, G. C., Shelly, D. R., & Uchide, T. (2007). A scaling law for slow earthquakes. *Nature*, *447*(7140), 76–79. https://doi.org/10.1038/nature05780
Ito, Y., Obara, K., Shiomi, K., Sekine, S., & Hirose, H. (2007). Slow earthquakes coincident with episodic tremors and slow slip events. *Science*, *315*(5811), 503–506. https://doi.org/10.1126/science.1134454
Jara, J., Bruhat, L., Thomas, M. Y., Antoine, S. L., Okubo, K., Rougier, E., et al. (2021). Signature of transition to supershear rupture speed in the coseismic off-fault damage zone. *Proceedings of the Royal Society A: Mathematical, Physical & Engineering Sciences*, *477*(2255), 20210364. https://doi.org/10.1098/rspa.2021.0364
Johnson, E. (1992). The influence of the lithospheric thickness on bilateral slip. *Geophysical Journal International*, *108*(1), 151–160. https://doi.org/10.1111/j.1365-246x.1992.tb00846.x
Kammer, D. S., Svetlizky, I., Cohen, G., & Fineberg, J. (2018). The equation of motion for supershear frictional rupture fronts. *Science Advances*, *4*(7), eaat5622. https://doi.org/10.1126/sciadv.aat5622
Katsumata, A., & Kamaya, N. (2003). Low-frequency continuous tremor around the Moho discontinuity away from volcanoes in the southwest Japan. *Geophysical Research Letters*, *30*(1), 20-1–20-4. https://doi.org/10.1029/2002gl015981
Knauss, W. G. (2015). A review of fracture in viscoelastic materials. *International Journal of Fracture*, *196*(1–2), 99–146. https://doi.org/10.1007/s10704-015-0058-6
Kovalyshen, Y., & Detournay, E. (2009). A reexamination of the classical PKN model of hydraulic fracture. *Transport in Porous Media*, *81*(2), 317–339. https://doi.org/10.1007/s11242-009-9403-4

Langer, J. S. (1992). Models of crack propagation. *Physical Review. A, General Physics*, *46*(6), 3123–3131. https://doi.org/10.1103/physreva.46.3123
Lapusta, N. (2001). *Elastodynamic analyses of sliding with rate and state friction* (Vol. 62–04B). Dissertation Abstracts International.
Lavier, L. L., Tong, X., & Biemiller, J. (2021). The mechanics of creep, slow slip events, and earthquakes in mixed brittle-ductile fault zones. *Journal of Geophysical Research: Solid Earth*, *126*(2), e2020JB020325. https://doi.org/10.1029/2020jb020325
Lehner, F. K., Li, V. C., & Rice, J. (1981). Stress diffusion along rupturing plate boundaries. *Journal of Geophysical Research*, *86*(B7), 6155–6169. https://doi.org/10.1029/jb086ib07p06155
Liu, Y., & Rice, J. R. (2005). Aseismic slip transients emerge spontaneously in three-dimensional rate and state modeling of subduction earthquake sequences. *Journal of Geophysical Research*, *110*(B8), B08307. https://doi.org/10.1029/2004jb003424
Liu, Y., & Rubin, A. M. (2010). Role of fault gouge dilatancy on aseismic deformation transients. *Journal of Geophysical Research*, *115*(B10), B10414. https://doi.org/10.1029/2010jb007522
Luo, Y., & Liu, Z. (2021). Fault zone heterogeneities explain depth-dependent pattern and evolution of slow earthquakes in cascadia. *Nature Communications*, *12*(1), 1959. https://doi.org/10.1038/s41467-021-22232-x
Lyakhovsky, V., Ben-Zion, Y., & Agnon, A. (2005). A viscoelastic damage rheology and rate- and state-dependent friction. *Geophysical Journal International*, *161*(1), 179–190. https://doi.org/10.1111/j.1365-246X.2005.02583.x
Mai, T. T., Okuno, K., Tsunoda, K., & Urayama, K. (2020). Crack-tip strain field in supershear crack of elastomers. *ACS Macro Letters*, *9*(5), 762–768. https://doi.org/10.1021/acsmacrolett.0c00213
Marder, M. (1998). Adiabatic equation for cracks. *Philosophical Magazine B*, *78*(2), 203–214. https://doi.org/10.1080/13642819808202942
Marder, M. (2005). Shock-wave theory for rupture of rubber. *Physical Review Letters*, *94*(4), 048001. https://doi.org/10.1103/PhysRevLett.94.048001
Michel, S., Gualandi, A., & Avouac, J.-P. (2019). Similar scaling laws for earthquakes and cascadia slow-slip events. *Nature*, *574*(7779), 522–526. https://doi.org/10.1038/s41586-019-1673-6
Nagatakiya, H., Sakumichi, N., Kobayashi, S., & Tarumi, R. (2023). Analytical expression for fracture profile in viscoelastic crack propagation. *arXiv preprint arXiv:1910.14547*.
Ng, E. W., & Geller, M. (1969). A table of integrals of the error functions. *Journal of Research of the National Bureau of Standards B*, *73*(1), 1–20. https://doi.org/10.6028/jres.073b.001
Obara, K. (2002). Nonvolcanic deep tremor associated with subduction in southwest Japan. *Science*, *296*(5573), 1679–1681. https://doi.org/10.1126/science.1070378
Palmer, A. C., & Rice, J. R. (1973). The growth of slip surfaces in the progressive failure of over-consolidated clay. *Proceedings of the Royal Society of London. A. Mathematical and Physical Sciences*, *332*(1591), 527–548.
Persson, B. N., & Brener, E. A. (2005). Crack propagation in viscoelastic solids. *Physical Review E - Statistical, Nonlinear and Soft Matter Physics*, *71*(3 Pt 2A), 036123. https://doi.org/10.1103/PhysRevE.71.036123
Petersan, P., Deegan, R., Marder, M., & Swinney, H. (2004). Cracks in rubber under tension exceed the shear wave speed. *Physical Review Letters*, *93*(1), 015504. https://doi.org/10.1103/PhysRevLett.93.015504
Rice, J. R., Sammis, C. G., & Parsons, R. (2005). Off-fault secondary failure induced by a dynamic slip pulse. *Bulletin of the Seismological Society of America*, *95*(1), 109–134. https://doi.org/10.1785/0120030166
Robertsson, J. O., Blanch, J. O., & Symes, W. W. (1994). Viscoelastic finite-difference modeling. *Geophysics*, *59*(9), 1444–1456. https://doi.org/10.1190/1.1443701
Rodriguez, N., Mangiagalli, P., & Persson, B. (2021). Viscoelastic crack propagation: Review of theories and applications. In *Fatigue crack growth in rubber materials: Experiments and modelling* (pp. 377–420).
Rubin, A., & Ampuero, J. (2005). Earthquake nucleation on (aging) rate and state faults. *Journal of Geophysical Research*, *110*(B11), B11312. https://doi.org/10.1029/2005jb003686
Ruina, A. (1983). Slip instability and state variable friction laws. *Journal of Geophysical Research*, *88*(B12), 10359–10370. https://doi.org/10.1029/jb088ib12p10359
Saulnier, F., Ondarçuhu, T., Aradian, A., & Raphaël, E. (2004). Adhesion between a viscoelastic material and a solid surface. *Macromolecules*, *37*(3), 1067–1075. https://doi.org/10.1021/ma021759t
Scholz, C. (1998). Earthquakes and friction laws. *Nature*, *391*(6662), 37–42. https://doi.org/10.1038/34097
Segall, P., Rubin, A. M., Bradley, A. M., & Rice, J. R. (2010). Dilatant strengthening as a mechanism for slow slip events. *Journal of Geophysical Research*, *115*(B12), B12305. https://doi.org/10.1029/2010jb007449
Seshadri, M., Saigal, S., Jagota, A., & Bennison, S. J. (2007). Scaling of fracture energy in tensile debonding of viscoelastic films. *Journal of Applied Physics*, *101*(9). https://doi.org/10.1063/1.2717550
Shibazaki, B., & Iio, Y. (2003). On the physical mechanism of silent slip events along the deeper part of the seismogenic zone. *Geophysical Research Letters*, *30*(9), 1489. https://doi.org/10.1029/2003gl017047
Suzuki, T., & Yamashita, T. (2009). Dynamic modeling of slow earthquakes based on thermoporoelastic effects and inelastic generation of pores. *Journal of Geophysical Research*, *114*(B6), B00A04. https://doi.org/10.1029/2008jb006042
Svetlizky, I., Bayart, E., & Fineberg, J. (2019). Brittle fracture theory describes the onset of frictional motion. *Annual Review of Condensed Matter Physics*, *10*(1), 253–273. https://doi.org/10.1146/annurev-conmatphys-031218-013327
Thøgersen, K., Aharonov, E., Barras, F., & Renard, F. (2021). Minimal model for the onset of slip pulses in frictional rupture. *Physical Review E*, *103*(5), 052802. https://doi.org/10.1103/PhysRevE.103.052802
Trottet, B., Simenhois, R., Bobillier, G., Bergfeld, B., van Herwijnen, A., Jiang, C., & Gaume, J. (2022). Transition from sub-Rayleigh anticrack to supershear crack propagation in snow avalanches. *Nature Physics*, *18*(9), 1094–1098. https://doi.org/10.1038/s41567-022-01662-4
Ujiie, K., Saishu, H., Fagereng, A., Nishiyama, N., Otsubo, M., Masuyama, H., & Kagi, H. (2018). An explanation of episodic tremor and slow slip constrained by crack-seal veins and viscous shear in subduction mélange. *Geophysical Research Letters*, *45*(11), 5371–5379. https://doi.org/10.1029/2018gl078374
Wang, M., Shi, S., & Fineberg, J. (2023). Tensile cracks can shatter classical speed limits. *Science*, *381*(6656), 415–419. https://doi.org/10.1126/science.adg7693
Weng, H., & Ampuero, J. (2019). The dynamics of elongated earthquake ruptures. *Journal of Geophysical Research: Solid Earth*, *124*(8), 8584–8610. https://doi.org/10.1029/2019jb017684
Weng, H., & Ampuero, J.-P. (2020). Continuum of earthquake rupture speeds enabled by oblique slip. *Nature Geoscience*, *13*(12), 1–5. https://doi.org/10.1038/s41561-020-00654-4
Weng, H., & Ampuero, J. P. (2022). Integrated rupture mechanics for slow slip events and earthquakes. *Nature Communications*, *13*(1), 7327. https://doi.org/10.1038/s41467-022-34927-w

10.1029/2024JB030663

Weng, H., & Yang, H. (2017). Seismogenic width controls aspect ratios of earthquake ruptures. *Geophysical Research Letters*, *44*(6), 2725–2732. https://doi.org/10.1002/2016gl072168

Willis, J. R. (1967). Crack propagation in viscoelastic media. *Journal of the Mechanics and Physics of Solids*, *15*(4), 229–240. https://doi.org/10.1016/0022-5096(67)90013-0

Wu, B. (2021). *Explaining slow earthquake phenomena with a frictional-viscous faulting model (Thesis)*. University of California.

Xu, D., Hui, C., & Kramer, E. J. (1992). Interface fracture and viscoelastic deformation in finite size specimens. *Journal of Applied Physics*, *72*(8), 3305–3316. https://doi.org/10.1063/1.352342

Yan, Y., Li, J., & Li, X. (2022). Dynamic viscoelastic model for rock joints under compressive loading. *International Journal of Rock Mechanics and Mining Sciences*, *154*, 105123. https://doi.org/10.1016/j.ijrmms.2022.105123

Zhang, H., Meng, H., & Ben-Zion, Y. (2023). Lateral variations across the southern san andreas fault zone revealed from analysis of traffic signals at a dense seismic array. *Geophysical Research Letters*, *50*(14), e2023GL103759. https://doi.org/10.1029/2023gl103759

Zhang, Q. B., & Zhao, J. (2013). A review of dynamic experimental techniques and mechanical behaviour of rock materials. *Rock Mechanics and Rock Engineering*, *47*(4), 1411–1478. https://doi.org/10.1007/s00603-013-0463-y